Dennis Matthews (in plaid shirt, far left) and the team of scientists and technicians who developed LLNL's laboratory x-ray laser. This photograph was taken in the summer of 1984, soon after the demonstration of the first x-ray laser at LLNL.

X-Ray Optics

Because of the extraordinary progress of the past decade, there now exist at soft x-ray wavelengths all the fundamental components necessary for a robust and successful optics technology.

In optics, one needs sources, lenses, mirrors, and detectors in order to perform useful tasks. The range and complexity of the tasks achievable depend in large part on the performance characteristics of those fundamental optical components. Imagine then, the impact of an optics technology in which the brightness of sources is increased by factors of one hundred million to a trillion, where the resolution of lenses is increased by a factor of about ten, where new mirrors that never existed are invented, and where detector speeds are increased a thousandfold! This has been the story of x-ray optics over the past decade or so.

High-Brightness Sources

In x-ray research applications, the characteristics of the x-ray source play a key role in defining what, in practical terms, can and cannot be done. Although sources can be characterized in many ways (e.g., coherence, spectrum, etc.), for our purposes we will focus on "brightness" and, in simple terms, "brighter" means "better." For example, in research, brighter sources will generally provide more information per experiment; in industry, they allow processes to be completed faster. The emergence of x-ray lasers and synchrotron insertion devices has increased the brightness of laboratory sources eight to twelve orders of magnitude over what was typically available in the late 1960s. The impact this will have on the technology of the future is probably greater than we can reasonably predict. For now we focus on the events of the recent past and the story of the technological development of these sources.

X-Ray Lasers

"If scientists using x rays have a dream, it must be of an x-ray laser... though immediate prospects for such a laser are slight..." A. L. Robinson, Science (1979).

Such is the nature of revolutions. In prospect they are invisible, in retrospect inevitable. Just five years after Arthur Robinson's article, not one but two teams jointly announced the achievement of the "*dream*." Although the timing of their accomplishments was virtually simultaneous, their approaches to the challenge of x-ray laser development were very different. (For a short description of lasing requirements, see "What is an X-Ray Laser?" on the facing page.)

LLNL X-Ray Laser Development

At LLNL, Dennis Matthews and his colleagues pursued a scheme involving collisional excitation of neon-like (and more recently nickel-like) ions. In fact, the first unequivocal demonstration of significant amplified spontaneous emission (ASE) occurred at LLNL using neon-like selenium. In this case, a thin (75-nm), Formvar-supported, selenium foil was irradiated by a short (0.45-ns), intense (5×10^{13}–W/cm^2) pulse of frequency-doubled (0.53-μm) neodymium laser light from the Nova laser. These early experiments produced hundreds of watts of ASE at 20.63 and 20.96 nm. The laser line emission emerged from a plasma column roughly 2 cm long and 100 μm in diameter; it had a divergence of 5–10 mrad and a duration of about 200 ps.

The kinetics of the neon-like selenium inversion scheme are illustrated in Figure 1. According to the calculational model, the laser irradiation of the target rapidly ionizes (in some hundreds of picoseconds) a significant fraction of the selenium atoms to the neon-like state ($Z = 10$) in a plasma with an electron temperature close to 1 keV and an electron density in the range 10^{20}–10^{21} electrons/cm^3. (These are the conditions presumed in Figure 1.)

Under these plasma conditions, the kinetics are quite favorable for the establishment of a population inversion between the $2p^53p$ and $2p^53s$ manifolds of the neon-like selenium ions. (A brief discussion of atomic configurations and transitions is highlighted on p. 10.) Collisional excitation of the $2p^53p$ levels from the $2p^6$ ground state is very rapid (~100 ps), whereas the radiative $2p^53p \rightarrow 2p^6$ decay is dipole-forbidden. In addition, the collisional excitation of the $2p^53s$ lower laser level is comparatively slow (~1 ns) and the $2p^53s \rightarrow 2p^6$ radiative decay is very rapid (~0.5 ps, in the absence of radiation trapping), ensuring the depopulation of the lower laser level. As shown in Figure 1, two possible $2p^53p \rightarrow 2p^53s$ transitions in the collisionally excited neon-like selenium ion are the $(1/2,3/2)_2 \rightarrow (1/2,1/2)_1$ transition at 20.96 nm and the $(3/2,3/2)_2 \rightarrow (3/2,1/2)_1$ transition at 20.63 nm. Both of these transitions produced intense levels of ASE in the early LLNL experiments.

At the time of the LLNL experiments, the theory underlying the collisional excitation of neon-like ions was already almost a decade old. The inversion scheme was first proposed by Soviet physicists in the 1970s. What was new and what allowed Matthews and his colleagues

What is an X-Ray Laser?

Laser light is electromagnetic radiation that is nearly monochromatic and highly directional. We say that such radiation is temporally and spatially coherent. Coherency is the characteristic that distinguishes laser light from ordinary light. Current sources of coherent radiation range in wavelength from microwaves, through the infrared and visible, into the extreme-ultraviolet and now into the soft-x-ray region of the electromagnetic spectrum.

In general, a laser consists of:

- An active lasing medium with energy levels that can be preferentially filled to create a population inversion (e.g., neon-like selenium in the LLNL experiments).
- A source of pumping energy to produce the excited states in the lasing medium.
- A resonant cavity that contains the lasing medium, stores the emitted coherent radiation, and repeatedly reflects the radiation through the medium until the inverted population is depleted, thus maximizing the amplification or gain (see "Research Applications," p. 30).

The functions of these basic components gave rise to the acronym *laser*: *l*ight *a*mplification by *s*timulated *e*mission of *r*adiation.

X-ray lasers differ from the more common optical lasers in that the electromagnetic radiation is emitted at a shorter wavelength (i.e., higher-energy lasing transitions), the laser technology is not as mature (e.g., temporal and spatial coherence is not as good as for optical lasers), and the x-ray lasers require much greater sources of pumping power (e.g., LLNL's Nova laser).

All lasing depends on producing a population inversion in the atoms, molecules, or ions of the lasing medium. In a population inversion, there are more atoms in high-energy quantum states than in low-energy states—the inverse of the normal energy distribution (see "Atomic Transitions," p. 10). When a high-energy electron spontaneously decays to a lower energy state, it emits a photon. If a population inversion exists, such photons can stimulate further emission in other atoms or ions of the lasing medium, producing a cascade effect. The intensity of the laser radiation resulting from this stimulated emission increases exponentially as the product of the gain and the length of the lasing medium.

There are many ways to create a population inversion, depending on the lasing medium used, the lasing wavelength, and other factors. The primary challenge is to pump the atoms (or ions) into the desired high-energy "excited" state more rapidly than the rate of spontaneous decay back down to lower-energy states. This has proved to be difficult at short (e.g., x-ray) wavelengths, because not only is the energy of the lasing transition greater but the spontaneous decay rates are also much more rapid. In fact, the pumping power required to overcome the spontaneous emission (and to produce a population inversion) scales as the transition energy (or inversely as the lasing wavelength) to the 9/2 power! This accounts for the use of high-power pump lasers to produce population inversions in the x-ray laser gain media.

to successfully exploit these ideas in 1984 was the existence of the high-power, short-pulse Nova laser coupled with LLNL experience in laser-produced plasmas. This combination of equipment and expertise permitted the production of the required high-density, high-temperature plasma over macroscopic dimensions and on a short enough time scale (~0.1 ns) to compete with the excitation and decay processes illustrated in Figure 1.

Early x-ray laser data from the LLNL experiments are presented in Figure 2. Shown are time-resolved imaging spectrometer data for four x-ray laser experiments, illustrating the variation of spectral radiant intensity with the length of the gain medium. Beneath each film data record is a linear plot of the x-ray spectrum taken at the peak of the x-ray emission. Features of interest in the data records are indicated by the letters A, B, C, D, E, W:

A. The $2p^63p \rightarrow 2p^63s$ transition in sodium-like selenium at 20.11 nm.

B. The $2p^53p(3/2,3/2)_2 \rightarrow 2p^53s(3/2,1/2)_1$ transition in neon-like selenium at 20.63 nm.

C. The $2p^53p(1/2,3/2)_2 \rightarrow 2p^53s(1/2,1/2)_1$ transition in neon-like selenium at 20.96 nm.

D. The $2p^53p(3/2,3/2)_1 \rightarrow 2p^53s(3/2,1/2)_1$ transition in neon-like selenium at 22.02 nm (not shown in Figure 1).

E. The second-order absorption edge of the beryllium filter, used as a wavelength fiducial at 22.2 nm.

W. The shadow of a wire used as a spatial resolution fiducial.

Of particular interest in Figure 2 is the nonlinear increase in intensity of the neon-like laser lines (B, C) relative to the sodium-like line (A). For the 5-mm target (Figure 2a), lines A, B, and C are of similar intensity. For the longer targets (11 mm, Figure 2b; 16 mm, Figure 2c), transitions B and C have significantly increased in intensity, whereas the intensity of the sodium-like line (A) is virtually unchanged (it is optically thick). For the 21-mm target (Figure 2d), the signal had to be heavily filtered to keep the neon-like lines (B, C) within the dynamic range of the streak camera. On that scale, the sodium-like line (A) is hardly discernible.

Extensive work has been done at LLNL in exploring the limits of the neon-like selenium laser and

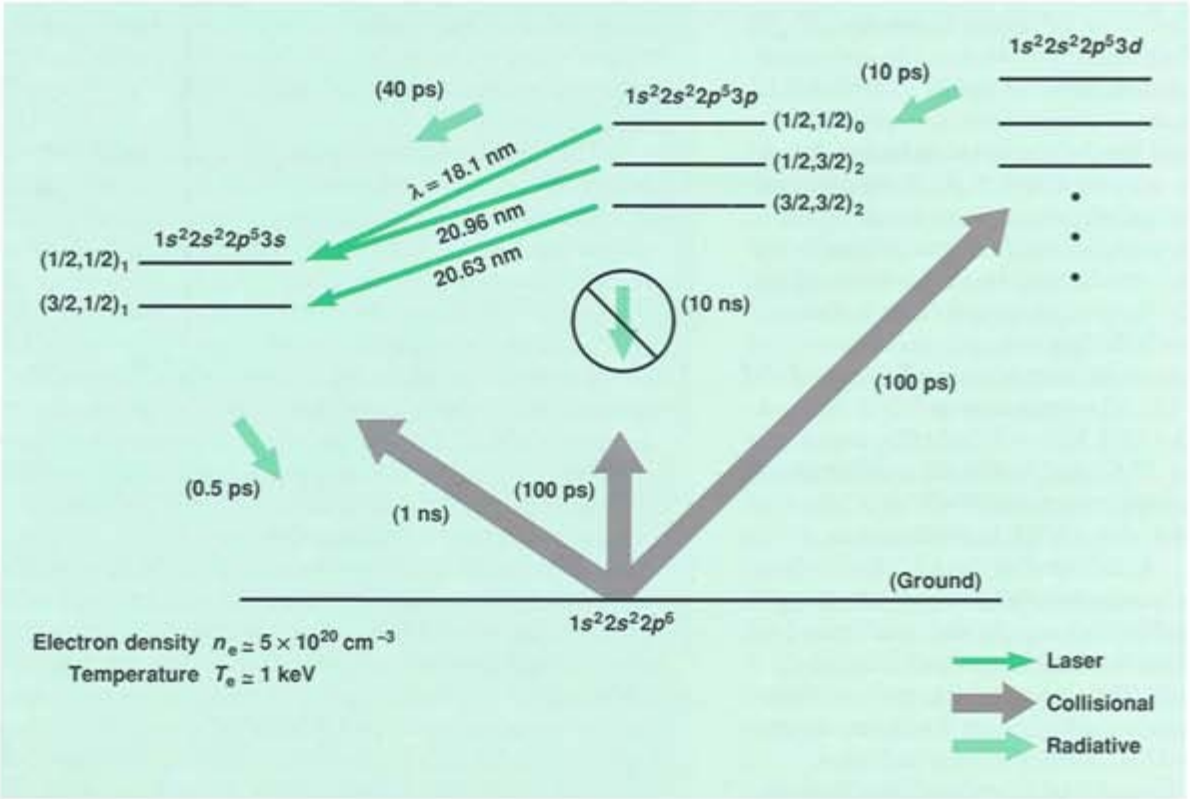

Figure 1. Simplified kinetics for the population inversion scheme involving collisionally excited neon-like selenium. In the LLNL experiments, the Nova laser was used to produce a plasma with the density and temperature shown. Under these conditions, a population inversion and ASE at 20.63 nm and 20.96 nm were produced.

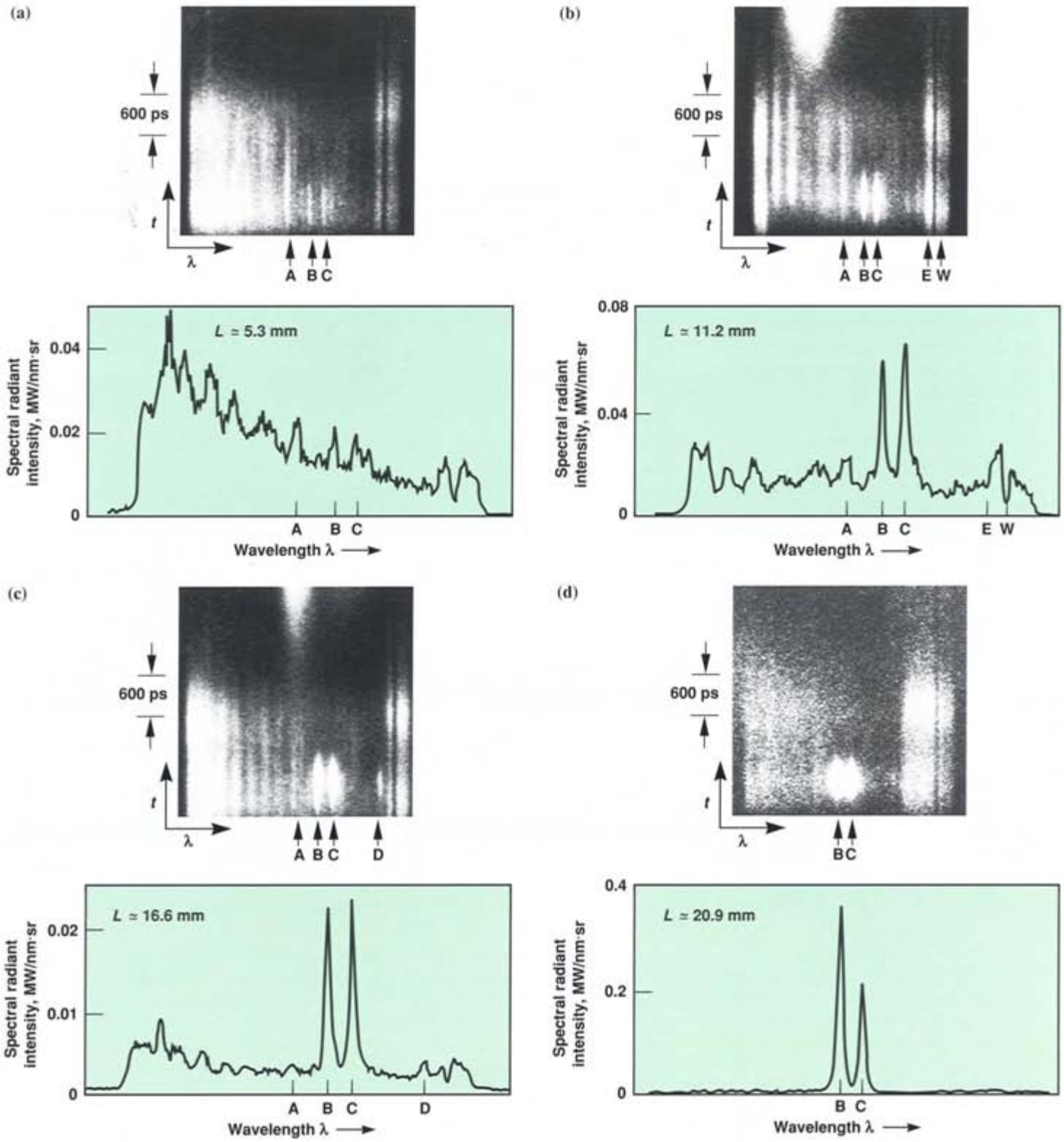

Figure 2. Time-resolved imaging spectrometer data for four different x-ray laser experiments with four different target lengths (L): 5.3 mm, 11.2 mm, 16.6 mm, and 20.9 mm. Below each data set is plotted the spectral radiant intensity at the time of peak emission. Note that A (the optically thick 20.11-nm sodium-like line) is virtually unchanged as target length is varied, whereas B and C (the laser lines at 20.63 nm and 20.96 nm, respectively) increase nonlinearly as target length is varied. E and W are wavelength and spatial resolution markers.

Atomic Transitions

The electronic transitions in ionized atoms that produce x-ray laser radiation can be visualized most simply by consideration of the Bohr model of the atom. In this model, the atom is represented by a nucleus of positive charge surrounded by negatively charged electrons that occupy well-defined, stable, circular orbits. The nuclear charge is equal to $+Ze$ where Z is the atomic number of the element (e.g., $Z = 34$ for selenium) and e is the fundamental unit of electron charge ($e = 1.6 \times 10^{-19}$ C).

The orbiting electrons occupy shells and subshells that are designated by the quantum numbers n, l of the stable orbital configurations. In this simple model, n designates the orbital shell number and is the primary determinant of electron energy; l designates the orbital subshell number and represents the orbital angular momentum of the electron. For example, the ground state of neon-like selenium (illustrated in the adjacent figure) has an atomic number $Z = 34$ and 10 orbiting electrons. The electrons are distributed in subshells as follows: 2 electrons in the 1s shell ($n = 1$, $l = 0$), 2 electrons in the $2s$ subshell ($n = 2$, $l = 0$), and 6 electrons in the $2p$ subshell ($n = 2$, $l = 1$). Thus the $1s^2 2s^2 2p^6$ designation for the ground state of neon-like selenium.

Energy is absorbed or emitted by the atom in distinct, quantized units that correspond to changes in the electron orbital configuration from one stable or "allowed" configuration to another. For example, the transition $2p^5 3p \rightarrow 2p^5 3s$ represents a single electron moving from the $3p$ ($n = 3$, $l = 1$) subshell to the $3s$ ($n = 3$, $l = 0$) subshell, with a release of energy (in the form of a photon) corresponding to the energy difference between these two stable states.

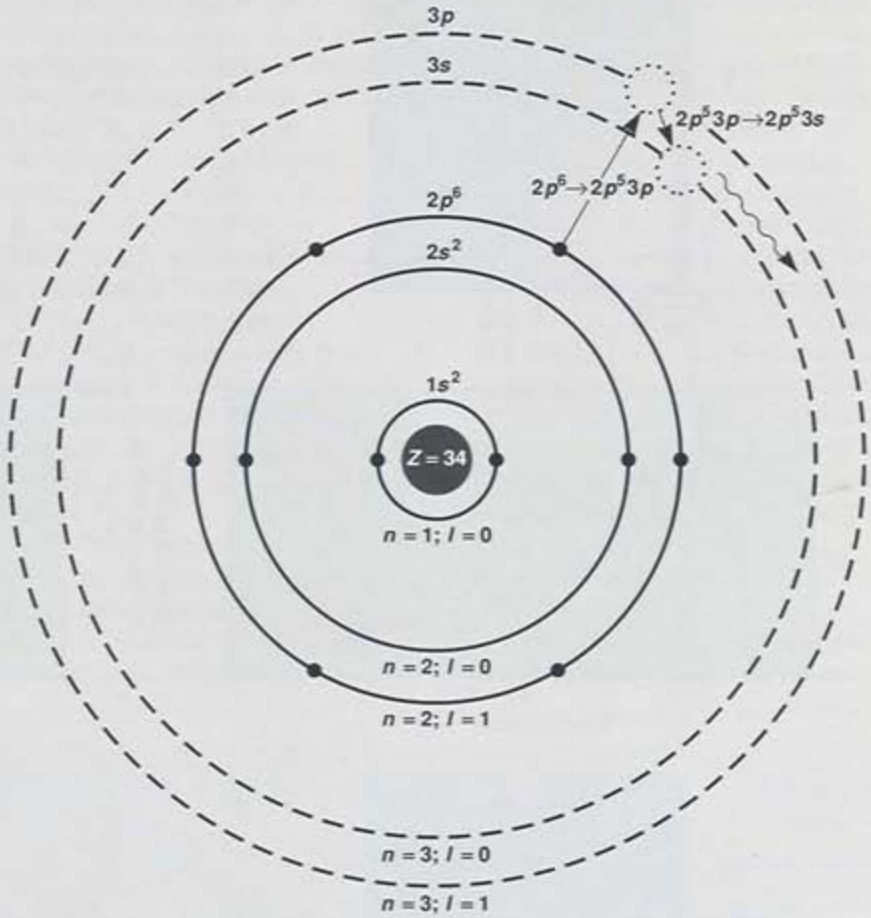

In order to determine the precise energy released in such a transition (and thus the wavelength of the emitted photon), one must go beyond the simple planetary Bohr model of the atom and consider in detail the energy of the atomic system before and after the transition. The precise energy of an atomic configuration depends in part on its angular momentum. Indeed, it is the angular momentum of the electron configuration that is designated by the notation $(j_1,j_2)_J$ used in Figure 1. In this notation, j_2 is a quantum number representing the angular momentum of the "active" electron involved in the transition; similarly, j_1 represents the net angular momentum of the core of "inactive" electrons. J represents the total angular momentum of the system resulting from the vector addition of j_1 and j_2. Thus the laser transition at 20.96 nm, $(1/2,3/2)_2 \rightarrow (1/2,1/2)_1$, occurs when the active electron undergoes an angular-momentum change from $j_2 = 3/2$ to $j_2 = 1/2$, resulting in an overall system angular-momentum change from $J = 2$ to $J = 1$ and the emission of a photon at a wavelength of 20.96 nm.

attempting to extend the scheme to shorter wavelengths by isoelectronic scaling to higher-Z materials. Progress along these lines is included in Table 1. The neon-like selenium system has been extended to gain-length products as high as 16 and output powers as high as 10^6 W. Significant ASE has also been produced at 16.41 and 16.65 nm in neon-like strontium and at 13.27, 13.1, and 10.64 nm in neon-like molybdenum. The kinetics for the neon-like strontium and molybdenum schemes are similar to the neon-like selenium shown in Figure 1. The primary difference is the larger separation between the energy levels of interest resulting from the increased atomic number (selenium $Z = 34$, strontium $Z = 38$, molybdenum $Z = 42$).

The extension of the collisional excitation scheme to neon-like ions of higher atomic number requires the production of plasmas with higher ionization state, electron density, and temperature. This in turn requires scaling the optical drive laser to significantly higher intensity, pushing the limits of currently available laser technology. For example, the 8×10^{12} W (4×10^{14} W/cm^2) needed to produce a gain-length product of 4 at 10.64 nm in neon-like molybdenum (see Table 1) approaches the limiting power available in two beams of the Nova laser.

This condition can be mitigated somewhat by going to collisional excitation of nickel-like ions, the

Table 1. Demonstrated performance of soft-x-ray lasers.

Wavelength, nm	Lasing medium	Demonstrated performance: Gain, cm^{-1}	Gain-length product (αL)	Output power, W	Laboratory
28.47 27.93	Neon-like copper	1.7	2.7	NM*	Naval Research Laboratory
23.63 23.22	Neon-like germanium	4.1	6.2	NM	Naval Research Laboratory
20.96 20.63	Neon-like selenium	4–6	16	~10^6	LLNL
18.2	Hydrogen-like carbon	6.5	6.5	~10^5	Princeton
16.65 16.41	Neon-like strontium	4.0 4.4	8.1 9.7	NM	LLNL, CEL-V (France)†
13.27 13.1	Neon-like molybdenum	4	7	~10^3	LLNL
10.64	Neon-like molybdenum	2	4	~10^2	LLNL
10.57	Lithium-like aluminum	1.0	2.0	NM	University of Paris
8.1	Hydrogen-like fluorine	5.5	2.8	NM	Rutherford Laboratory (U.K.)
7.1	Nickel-like europium	1.1	3.8	~10^2	LLNL, CEL-V (France)†
5.03	Nickel-like ytterbium	1.2	2.0	~10^2	LLNL, CEL-V (France)†

*NM = not measured.
†These measurements were made at the Centre D'Etudes de Limeil-Valenton, France, in a cooperative experimental effort between researchers at LLNL and CEL-V.

$4d \rightarrow 4p$ analog of the $3p \rightarrow 3s$ inversions of the neon-like scheme. This approach was first proposed by Peter Hagelstein and colleagues at LLNL. Since the nickel-like ions require less ionization (for a given Z), they are energetically easier to create in a laser-produced plasma. ASE has been produced and gain has been measured from collisionally excited nickel-like europium at 7.1 nm and nickel-like ytterbium at 5.03 nm using drive laser intensities of 7×10^{13} W/cm^2 and 2×10^{14} W/cm^2, respectively (roughly the same intensities required to pump the neon-like selenium and molybdenum lasers).

The kinetics for nickel-like systems are illustrated in Figure 3 for europium; the diagram has been simplified to emphasize its similarity to the neon-like scheme. In this case, a 600-eV plasma with an electron density of $\sim 2 \times 10^{20}$ cm^{-3}, produced by 7×10^{13} W/cm^2 of 0.53-μm laser light incident on a 50- to 90-μg/cm^2 europium fluoride foil, provides favorable conditions for a population inversion between the $3d^94d$ and $3d^94p$ manifolds of the nickel-like europium. This is achieved by the rapid collisional excitation of the $3d^94d$ levels and the rapid radiative depopulation of the $3d^94p$ levels, as in the neon-like inversion schemes.

A disadvantage of the nickel-like scheme is its typically lower gain, due to the smaller fraction of nickel-like ions that can be produced in an optimized laser-produced plasma. The more stable electronic configuration of neon-like ions allows the production of an optimized laser-produced plasma with an ion population that is roughly 50% neon-like. This has not yet been achieved for nickel-like ions.

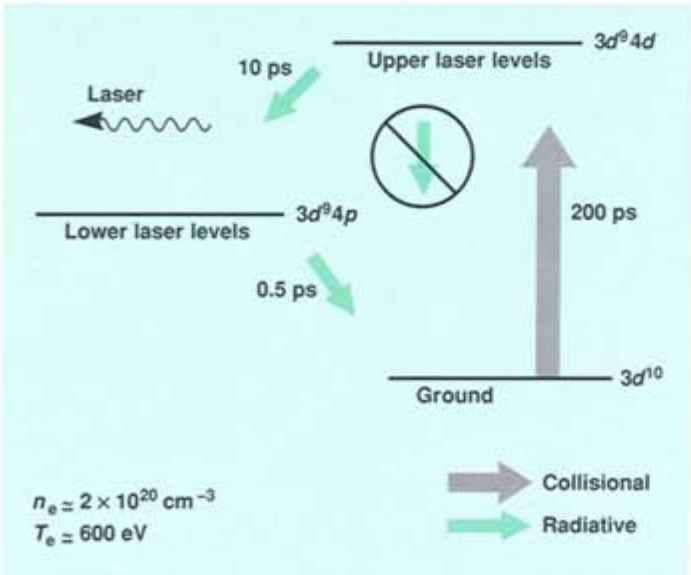

Figure 3. Simplified kinetics for the population inversion scheme involving collisionally excited nickel-like europium. The kinetics are analagous to those for neon-like selenium (Figure 1), leading to population inversions between 4*d* and 4*p* levels at a plasma temperature of only 600 eV.

Princeton X-Ray Laser Program

At Princeton University, Szymon Suckewer and his colleagues pursued an inversion scheme utilizing three-body recombination in hydrogen-like carbon, C(VI). They used an intense burst of CO_2 laser radiation upon a carbon target to produce a plasma of fully stripped carbon ions within a magnetic field, thereby creating a population inversion between the $n = 3$ and $n = 2$ levels of the carbon and producing ASE at 18.2 nm.

The recombination scheme pursued at Princeton is not new. Twenty-five years ago, Gudzenko and Shelepin first proposed the rapid creation of an appropriate high-density, high-temperature, fully ionized plasma, and the subsequent rapid cooling of the plasma to produce a nonequilibrium condition leading to a (three-body) recombination-pumped population inversion between the $n = 3$ and $n = 2$ levels of the hydrogenic ions.

Such recombination schemes are attractive because of the rapid isoelectronic scaling to shorter laser wavelength with increased atomic number Z of the host ion. On the other hand, there are great difficulties in creating and maintaining the macroscopic, high-density, uniform column of C(VI) ions while rapidly cooling them to produce the desired population inversion. Suckewer's solution to this problem was to create the carbon plasma within a strong solenoidal magnetic field. The field confines the plasma, thereby maintaining a high density and a rapid recombination rate ($\sim n_e^2$) while rapid radiative cooling ($\sim Z^4$) "freezes out" the populations of the lower levels, leading to the inversion.

In the Princeton experiments, a 300-J CO_2 laser emitting an intense ($\sim 5 \times 10^{12}$-W/cm^2), 75-ns burst of 10.6-μm radiation produced the carbon plasma within a solenoidal

magnetic field ($B = 90$ kG). Measurements indicate that the recombining plasma had an electron density, $n_e \sim 5 \times 10^{18}$ cm^{-3}, temperature $T_e \sim$10–20 eV, and an upper laser level population $n_i \sim 10^{15}$ cm^{-3}. The measured gain was ~6.5 cm^{-1} over a plasma length of approximately 1 cm. Estimates of the laser emission characteristics indicate an output power of roughly 10^5 W over a 10- to 30-ns duration, emerging with a divergence of about 10 mrad from a 50- to 100-μm-wide, 2.8-mm-diam annular region of the carbon plasma.

X-Ray Laser Research at Other Laboratories

In addition to the early x-ray laser success at LLNL and Princeton, there are more recent reports of the observation of significant ASE at a number of wavelengths, using a variety of inversion schemes, at a number of laboratories around the world (see Table 1). A team at the Naval Research Laboratory has reported the observation of ASE at 27.93 and 28.47 nm from neon-like copper and at 23.22 and 23.63 nm from germanium. O. Willi and coworkers in England have reported ASE at 8.1 nm from recombination-pumped hydrogen-like fluorine, while P. Jaegle and colleagues in France have observed laser activity at 10.57 nm from recombination in lithium-like aluminum ions.

The rapid progress in the proliferation of new x-ray laser lines and the extension to shorter x-ray wavelengths has been remarkable. In the space of four years, the observation of strong ASE and the measurement of gain has been extended from two lines around 20 nm to roughly two dozen lines extending down to 5 nm. If this extraordinary pace were to be maintained, then by the year 2000 ASE will have been observed on roughly 40,000 different lines extending down to wavelengths below 0.1 nm!

Synchrotron Insertion Devices

X-ray lasers are extraordinarily bright sources of extreme-ultraviolet (XUV) and soft-x-ray radiation (see Figure 4 on p. 14). They have great potential for temporal and spatial coherence, and their future impact in x-ray optics is hard to overestimate. Nevertheless, most of the x-ray laser systems are still in research and development stages, limited to wavelengths greater than 5 nm and not yet tunable. For the near term, we must look to more "conventional" sources of x radiation. Among these, the most significant recent advance in x-ray sources is the emergence of magnetic insertion devices (wigglers and undulators).

Wigglers and undulators are periodic magnetic structures designed to enhance the production of radiation from the electrons circulating in a synchrotron storage ring. Since the primary function of bending magnets in a storage ring is to maintain the beam in a closed and stable orbit, it should not be surprising that magnetic structures can be designed that are more effective in tailoring the synchrotron radiation to the specific needs of the user. Wigglers (or undulators) are typically placed in a straight section of the storage ring and are designed to produce no net deflection or displacement of the circulating beam. They enhance the brightness, extend (or narrow) the radiation spectrum, and modify the spatial and temporal coherence of the beam. (See p. 15 for a more quantitative discussion of synchrotron insertion devices.)

Wigglers and undulators use similar magnet technology. They are both high-field, periodic, linear magnet arrays through which the relativistic electron beam undergoes an oscillatory horizontal motion (i.e., in the plane of the circulating beam) under the influence of alternating vertical magnetic fields. Typically, undulators have many more periods, are fabricated to higher spatial and magnetic tolerances, and restrict the beam oscillations to smaller angular excursions than do wigglers. (In a typical undulator, the angular excursions of the oscillating beam are smaller than the natural emission angle of the synchrotron radiation, given by $1/\gamma$ where γ is the electron energy divided by its rest energy. In a wiggler, the angular excursions are much greater than the natural emission angle.)

The essential difference between wiggler and undulator operation is in the correlation of the emissions from the different poles of the magnetic structure. In a wiggler, the emissions are uncorrelated, so that the wiggler emission is roughly equivalent to $2N$ times that from a bending magnet with an equivalent magnetic field, where N is the number of periods (two poles or oscillations per period). Wiggler spectra typically extend to higher energies than do bending magnet spectra, simply because wiggler magnetic fields typically are stronger than bending magnet fields. In an undulator, the magnetic structure and beam are tuned so that the emissions from each period of the undulator are in phase (highly

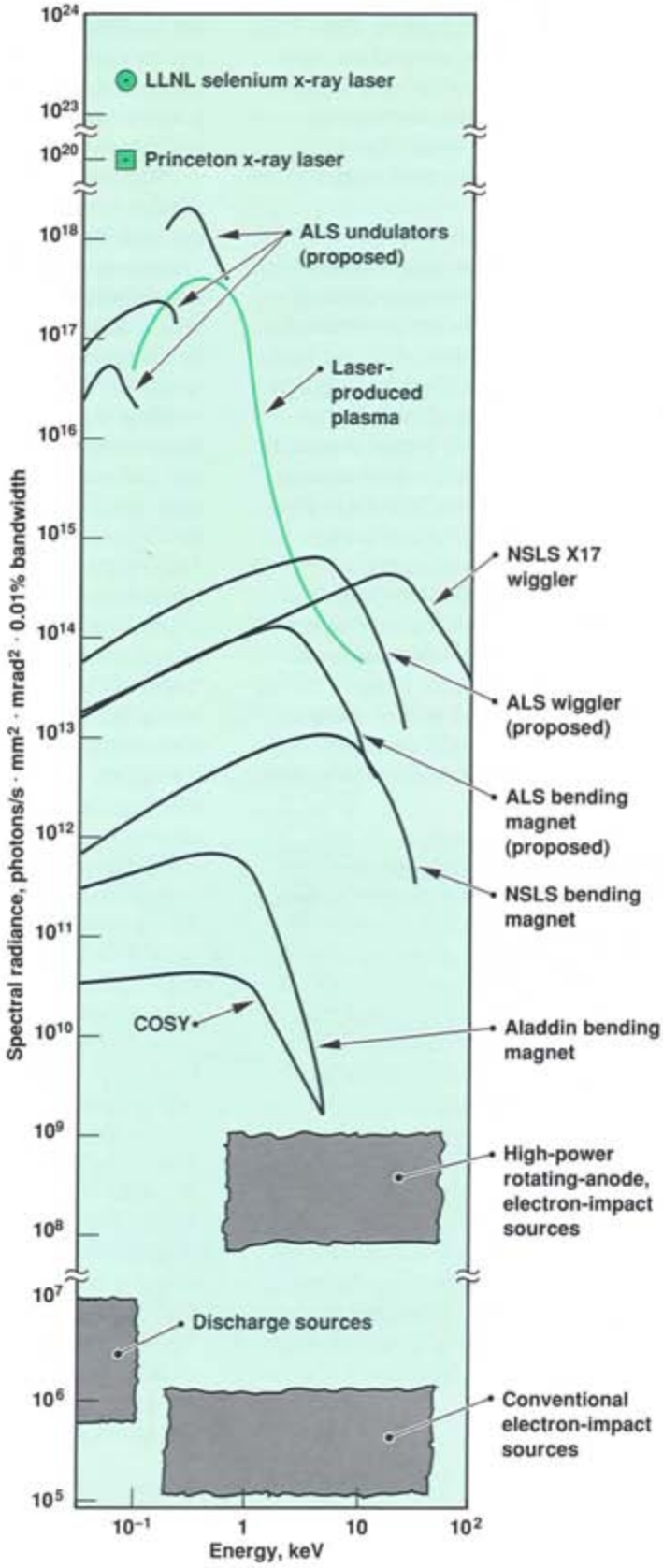

Figure 4. The extraordinary advance in x-ray source capabilities is illustrated. Spectral radiance (photons/ s · mm² · mrad² · 0.01% bandwidth) of bending magnet, wiggler, and undulator beamlines (black) are compared with the more conventional laboratory sources (gray) that dominated x-ray research in the late 1960s and early 1970s (discharges, electron impact on stationary and rotating anodes), and with the new high-power, laser-driven x-ray sources (green) currently under development (x-ray lasers and laser-produced plasmas). For the laser-driven sources, peak values are shown, whereas for the other sources average values are shown. (Note: two new wiggler beamlines at SSRL have a performance similar to the NSLS X17 shown here. LLNL has led the construction and operation of the new beamlines on behalf of the University of California and the National Laboratories' Research Team.)

correlated). As a result, the undulator emission is brighter (by roughly N^2) than that from an equivalent bending magnet. The correlation between pole emissions also serves to narrow the undulator spectrum, $(\lambda_0/\Delta\lambda) \sim N$. The fundamental undulator wavelength λ_0 is just the relativistically contracted undulator period, i.e., $\lambda_0 \sim p_u/2\gamma^2$, where p_u is the period of the magnetic undulator structure.

The evolution of x-ray sources over the past 20 years has been dramatic. Figure 4 compares the spectral radiance (photons/ s · mm² · mrad² · 0.01% bandwidth) of selected bending magnet, wiggler, and undulator beamlines with that of the more conventional laboratory sources that dominated x-ray research in the late 1960s and early 1970s (discharges, electron impact on stationary and rotating anodes) and with the new high-power, laser-driven x-ray sources currently under development (x-ray lasers and laser-produced plasmas). Table 2 presents more information on the various x-ray sources given in Figure 4.

We caution that such a single-parameter comparison of different x-ray sources can be misleading because their time duration, duty cycle, spectral bandwidth, source size, and divergence are all quite different. A judicious (or manipulative) choice of comparative parameters can make one type of source appear to be better than another. For example, the spectral-radiance parameter shown in Figure 4 favors intense sources of short duration but low duty cycle, such as laser-produced plasmas and x-ray lasers, and is somewhat less favorable for quasi-continuous sources, such as synchrotrons. To effectively compare x-ray sources, it is generally best to start with a particular experiment or application

of interest, define the source characteristics desirable for that application, and then assess the suitability of the various sources to the application. Nonetheless, the spectral-radiance curves in Figure 4 provide a gauge of progress in x-ray source technology in recent years.

The synchrotron radiation sources introduced in the early 1970s provided an increase in spectral radiance of two to four orders of magnitude over conventional x-ray sources; these machines had spectral radiance numbers in the range of the modern compact storage ring COSY (*co*mpact *sy*nchrotron) in Figure 4. Newer storage-ring facilities (e.g., Brookhaven's National Synchrotron Light Source or NSLS, currently in operation, and the Advanced Light Source or ALS at Lawrence Berkeley Laboratory, under construction) provide another two to three orders of magnitude in spectral brilliance. Wiggler and undulator insertion devices provide an additional two to four orders-of-magnitude increase in spectral brilliance, with the concomitant modification of source spectrum.

Although insertion-device concepts have been around since the 1940s and 1950s, they were first used in synchrotrons in the late 1970s and are only now becoming commonplace at storage-ring facilities around the world. The newly designed undulator beamlines proposed for the ALS will be ten to twelve orders of magnitude brighter than the conventional x-ray sources

Table 2. **Comparison of characteristic values of x-ray sources shown in Figure 4.**

Source type	Duration	Spectrum	Source size	Divergence	Output	Bandwidth
Hollow cathode discharge	Continuous	Multiline; varies with discharge gas	1 mm^2	~100 × 100 mrad	~10^{10}–10^{11} photons/s, per line	Assumed narrow (~10^{-4} λ)
Conventional (electron or proton) impact source	Continuous	Characteristic line emission	~5 × 5 mm	2π sr	~10^{13}–10^{14} photons/s per line into 2π sr	Assumed narrow (~10^{-3} to 10^{-4} λ)
Rotating anode impact source	Continuous	Characteristic line emission	10–100 mm^2	2π sr	1–10 W/mm^2	Assumed narrow (~10^{-3} to 10^{-4} λ)
LLNL selenium x-ray laser	~200-ps pulse	Single or few narrow lines	~0.1 × 0.1 mm	~5-mrad cone angle	10^{-4} J/pulse (maximum)	Assumed narrow (~10^{-4} λ)
Princeton x-ray laser	~10 ns	Single narrow line	~0.1-mm annular ring, of radius 1.4 mm	~10-mrad cone angle	~10^5 W	Assumed narrow (~10^{-4} λ)
Laser-produced plasma	~1 ns	Quasi-continuous	~0.1 × 0.1mm	2π sr	2 × 10^6 W/sr (peak)	Broad
Synchrotron sources:						
COSY	Quasi-continuous	Continuous	~10 mm^2	~1 mrad × 2π	~5 × 10^5 W/sr (average)	Broad
NSLS, ALADDIN	Quasi-continuous	Continuous	*	*	*	*
ALS	Quasi-continuous	Continuous	*	*	*	*

*See R. Garret, *Synchrotron Radiation News* **1**, 13 (1988).

Synchrotron Insertion Devices

To enhance the synchrotron radiation output (intensity and spectrum) without perturbing the stored beam, a magnetic insertion device is used. This device is a periodic magnetic structure with an on-axis vertical magnetic field of the form:

$$B_y(z) = B_0 \cos(2\pi z/p) ,$$

where y is the vertical direction, z is the direction of electron propagation around the ring, and p is the period of the magnetic structure. In such a device, the electron trajectory is purely horizontal; its transverse velocity is given by

$$v_x/c = K\gamma^{-1} \sin(2\pi z/p) ,$$

and its displacement by

$$x = pK(2\pi\gamma)^{-1} \cos(2\pi z/p) ,$$

where c is the velocity of light, γ is the ratio of the electron energy divided by its rest energy, and K is an important dimensionless parameter giving the ratio of the peak angular deviation of the electron trajectory to the unaltered synchrotron radiation cone angle γ^{-1}. K is given by

$$K = 0.934\, B_0 p ,$$

where B_0 is the on-axis magnetic field peak value in teslas and p is in centimeters.

Insertion devices are typically classified according to their K values. An undulator has small K (and typically many periods); a wiggler has large K (and typically fewer periods). Undulators and wigglers emit radiation with significantly different angular and spectral characteristics. For example, for $K >> 1$ (the wiggler limit), an on-axis observer sees radiation emitted toward him only twice each period when the electron's velocity is directed toward him. However, if $K < 1$ (the undulator limit), the angular excursions of the electron are small, and the same observer sees radiation emitted toward him along the entire extent of the undulator.

The observed spectra and angular divergence of the radiation are quite different in the two limiting cases. For $K >> 1$ (wiggler limit), the spectrum looks very much like that generated by a bending magnet, so the usual critical energy formula holds,

$$E_c = 0.665\, E^2 B ,$$

where E_c is the critical energy of the emitted x-ray spectrum (in keV), E is the electron energy (in GeV), and B is the magnetic field (in teslas) experienced by the electron when its velocity is directed toward the observer. In the wiggler limit, there is no interference between the radiation emitted at one point and its conjugate point in the N-periodic motion, so the observed flux is simply $2N$ times that from a bending magnet of field B. The horizontal angular spread of the wiggler radiation from an electron is $2K\gamma^{-1}$.

For $K < 1$ (undulator limit), the emission characteristics are dominated by interference effects along the N periods of the insertion device. Constructive interference (in first order) takes place at the resonant wavelength for which the light moves one period ahead of an electron as the electron crosses a single period of the undulator. (For the nth-order resonant wavelength, the light moves n periods ahead of the electron). For an on-axis observer, the resonant wavelength (in first order) is

$$\lambda_0 = p\gamma^{-2}(1 + K^2/2) ,$$

emitted into a radiation cone angle $\sim 2/\gamma(N)^{1/2}$, where N is the number of undulator periods. In the undulator limit, the spectral intensity of the undulator radiation is proportional to N^2, and the spectral bandwidth of the emission is narrowed to $\Delta\lambda \sim \lambda_0/N$, so the longitudinal coherence length is $\sim N\lambda_0$. The transverse coherence of the undulator emission depends on the emittance of the storage ring.

available for x-ray research in the early 1960s. On this scale, laser-produced plasmas have similar spectral radiance numbers, and the Princeton and LLNL x-ray lasers are a further two to five orders of magnitude greater.

These extraordinary advances in source brightness are making possible whole new classes of applications and experimental investigations. For example, a landmark demonstration of high-resolution (<1-μm) holography at soft-x-ray wavelengths was done in 1989 at Brookhaven using the newly completed undulator beamline at NSLS, and the first flash x-ray hologram was made at LLNL in 1988 using the newly developed selenium x-ray laser.

Optical Components

The development of optical components for the manipulation of soft x rays has been remarkably rapid in recent years. This effort has been motivated by a multi-disciplinary interest in short-wavelength radiation, and has benefitted from the exploitation of the thin-film deposition and nanometer-scale lithography technologies that were developed by the semiconductor electronics industry for the manufacture of high-density integrated circuits.

Fresnel Lensing Elements

Fresnel zone plate lenses are being developed for x-ray microscopy of live microbiological specimens, for applications in solid state and surface physics, and for integrated-circuit mask inspection in x-ray lithography. The rapid advance in Fresnel lens fabrication has resulted primarily from the application of advanced electron-beam lithographic systems recently developed for the production of integrated circuits.

A Fresnel zone plate pattern is illustrated in Figure 5. It is a circularly symmetric array of annular zones that are alternately transparent and opaque. The concentric circles defining the successive annuli have radii r_n given by

$$r_n^2 = n\lambda f + n^2 (\lambda^2/4), \quad n = 1, 2, 3, \ldots, N,$$

where f is the focal length of the lens, λ is the x-ray wavelength, and n is the zone number. Fresnel lensing structures provide the potential for diffraction-limited x-ray imaging with a spatial resolution (in first order) approaching the dimension of the minimum (i.e., outermost) zone width.

Since it is a diffractive imaging element, a Fresnel lens has many imaging orders. Diffraction efficiency into first order is ≤10% for zone-plate and ≤40% for Fresnel phase-plate structures. (A Fresnel phase plate has the same geometrical zone structure as a zone plate. It achieves improved efficiency by replacing the opaque zones (which absorb x rays) with transparent,

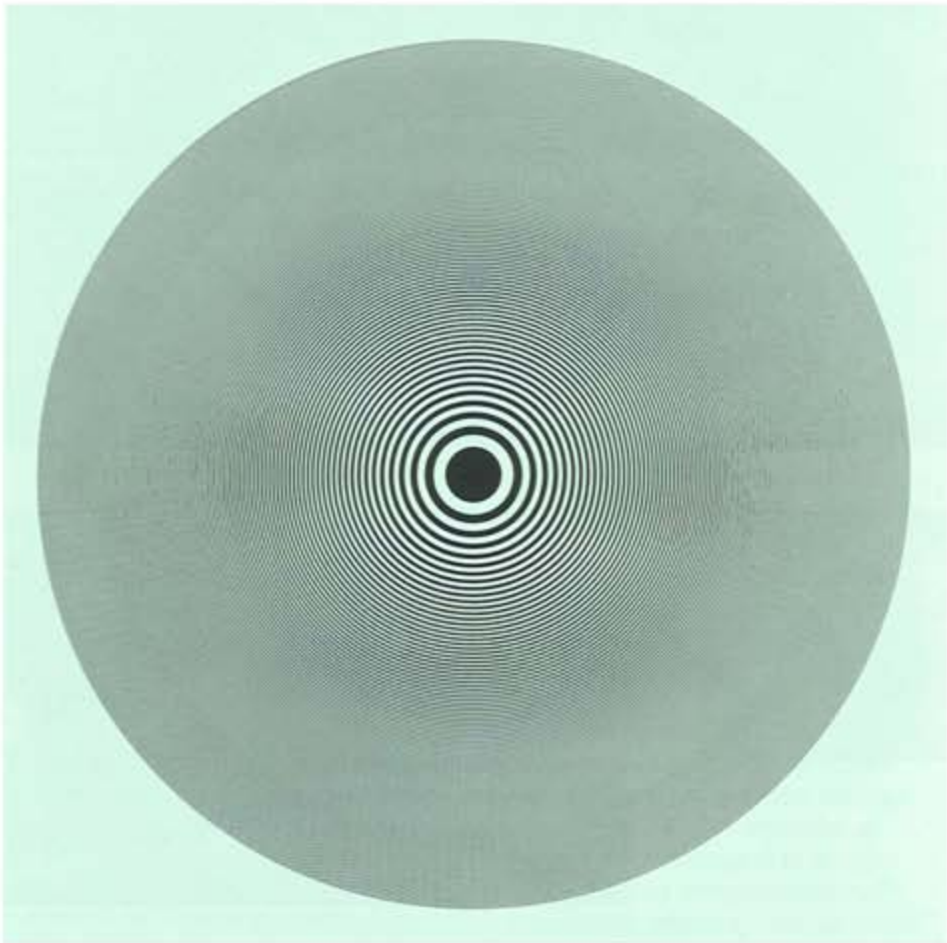

Figure 5. A Fresnel zone plate pattern. Such a pattern of equi-area annular rings may be used to focus x rays by diffraction. The limiting focal spot size is equal to the width of the outermost zone.

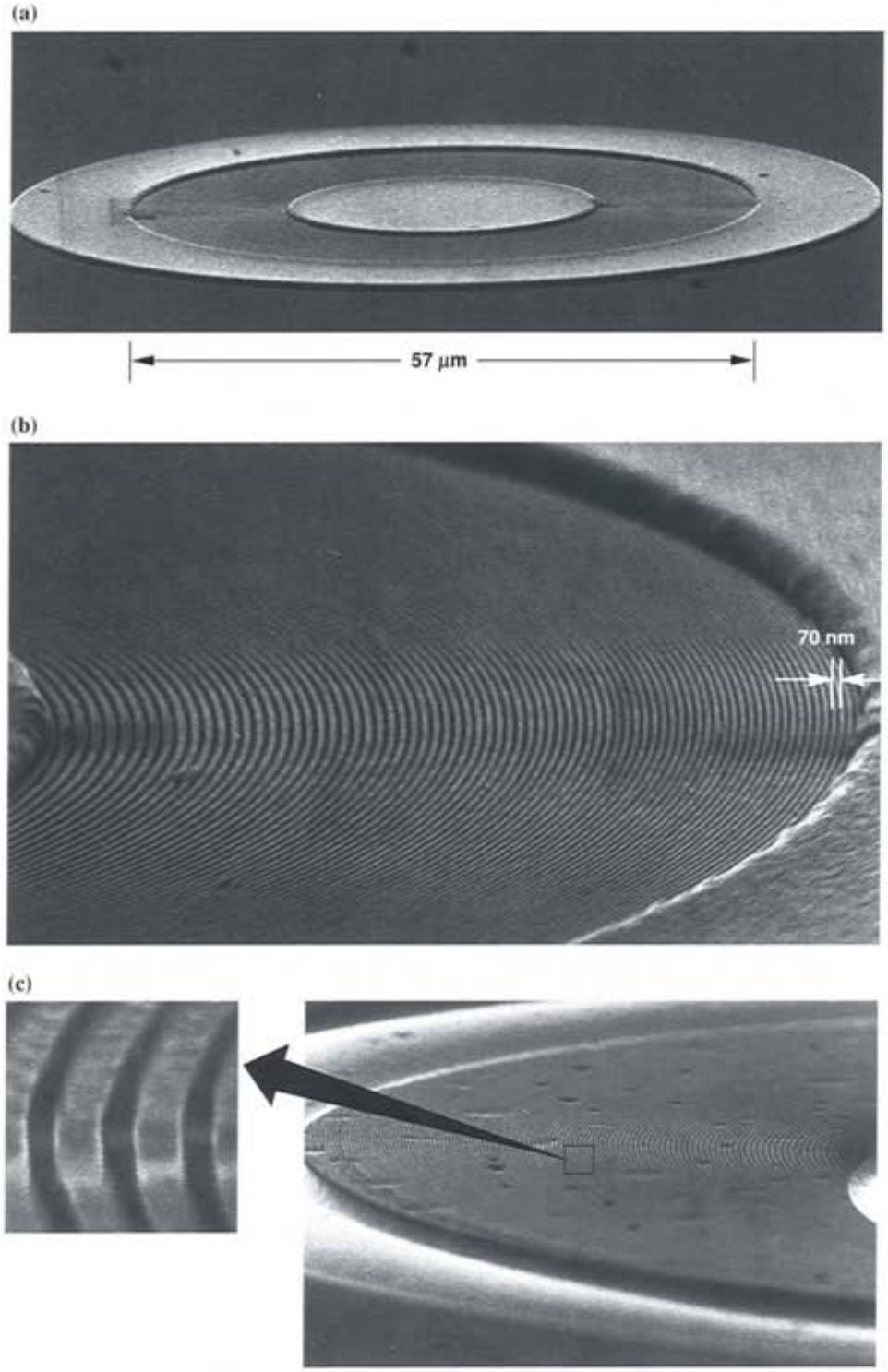

Figure 6. State-of-the-art Fresnel zone plates fabricated by electron beam lithography. (a) Full view of a zone plate with outermost zone width (Δr) equal to 70 nm. Note the opaque (gold) apodizing central region. (b) A magnified view of the zone plate shown in (a). (c) A Fresnel zone plate with $\Delta r \approx 50$ nm. (Courtesy of Y. Vladimirsky, IBM.)

phase-shifting zones. A relative phase shift of π is required to optimize the first-order diffraction efficiency).

Higher order images may also be utilized. They have the advantage of improved resolution, but the diffraction efficiency into higher order decreases as the square of the order number.

Narrow-linewidth Fresnel structures are currently being fabricated at a number of facilities throughout the world. Zone plates with minimum zone widths of 70 and 50 nm (see Figure 6) have been fabricated by Vladimirsky at IBM and are operating as objective lenses in experimental x-ray microscopes covering a spectral range from 3 to 4.5 nm. These microscopes report resolutions approaching 50 nm in the imaging mode, and 75 nm in the scanning mode. More recently, Fresnel zone plates with 40-nm minimum zone widths have been used in an imaging microscope at 4.5 nm for the inspection of integrated circuit masks; a spatial resolution approaching 40 to 50 nm was reported.

Work is under way at these same facilities to fabricate the next generation of Fresnel zone-plate structures with minimum zone widths as small as 10 nm. The narrower zone width provides better image resolution and improved lens speed.

The rapidly advancing pace of microfabrication technology provides the prospect of diffraction-limited imaging and focusing on the scale of the wavelength of soft x rays, albeit with some limitation on diffraction efficiency.

Multilayer Mirrors

After high-resolution lenses, the most important development in soft-x-ray optical components has been

the production of efficient, normal-incidence multilayer reflection optics. The ability to reflect x rays at normal incidence (90°) simplifies the optical design for radiation and image transfer systems and allows the realization of sophisticated optical techniques such as interferometry, Fourier-transform holography, and diffraction-limited projection (i.e., reduction) imaging for applications such as x-ray lithography.

A multilayer x-ray mirror is the analog of a quarter-wave stack reflective coating with the added complication of radiation absorption in the layers. Physically, it is an alternating sequence of thin films of highly absorbing and less-absorbing materials deposited on an optically smooth substrate. Typically, the layered structure is periodic (although this is not essential) and results in a large-angle, resonant reflectivity three to four orders of magnitude greater than the simple Fresnel reflection from an unlayered surface. Reflectivity in a multilayer mirror derives from the interference of x rays coherently scattered from the interfaces between materials of higher and lower x-ray absorption. Maximum constructive interference occurs when the resonant Bragg condition,

$$m\lambda = 2d\mu \sin\theta ,$$

is satisfied, where λ is the vacuum-x-ray wavelength, m is the order number, d is the period for the layer pair, μ is a refractive correction term,[1] and θ is the angle of incidence measured from the mirror surface ($\theta = 90°$ at normal incidence).

At resonance, the x-ray absorption losses in the multilayered structure are considerably less than would be expected from the simple passage of x rays through the integrated thickness of the mirror material. This is because the Bragg condition is equivalent to establishing a resonant standing wave in the multilayer with the highly absorbing layers located precisely at the nodes and the less absorbing layers at the anti-nodes of the standing wave. Under these conditions, the probability of finding an x-ray photon in a highly absorbing layer, where it can be lost, is much smaller than in a less-absorbing layer, where its chance of survival is greater. So then, if a geometrically perfect structure could be fabricated with very thin absorbing layers and "spacer" layers of very low absorption, many layers could participate in the interference process with minimal losses, thereby producing efficient (albeit narrowband) mirrors with high reflectivity.

Although some early work was done in the 1930s on the use of metallic layered structures for use as x-ray reflectors, Troy Barbee (LLNL) and Eberhard Spiller (IBM) are generally recognized as the pioneers of modern multilayer mirror technology. Spiller is generally credited with the first (1972) sophisticated design of synthetic multilayered structures for use as versatile, efficient x-ray reflectors. Initial fabrication efforts in the mid-1970s produced x-ray mirrors that demonstrated the concept of multilayer reflectivity but did not achieve its potential. Because of technological limitations, these early multilayer mirrors had reflectivities far below their absorption-limited performance. However, in the early 1980s, Barbee and others pioneered significant advances in fabrication technology motivated by interest in superlattice structures and the need for high-precision, thin-film deposition for semiconductor and integrated circuit applications. At about the same time, new capabilities developed in the use of STEM (scanning transmission electron microscopy) characterization of multilayered structures and synchrotron x-ray characterization of mirror performance. These advances of the early 1980s laid the groundwork for the development of high-performance multilayer x-ray mirrors.

At LLNL, we have judiciously exploited these emerging technologies to produce normal-incidence multilayer mirrors for use with the newly developed soft-x-ray lasers. There are a number of groups at LLNL producing high quality x-ray mirrors: [e.g., Dan Makowiecki, Alan Jankowski, and Troy Barbee (Chemistry and Materials Science), and Peter Biltoff (Engineering), and Richard Bionta (Physics)]. The following paragraphs describe multilayer mirror fabrication in the Advanced X-Ray Optics Group within LLNL's Laser Fusion Program.

In this program, multilayer mirror fabrication and characterization follows a standard procedure. Once a wavelength and incidence angle have been chosen (e.g., 20.63 nm at normal incidence for an x-ray laser cavity), the appropriate multilayer mirror is designed, including materials, d spacing, γ (ratio of highly absorbing material thickness to d spacing), and N (number of layer pairs), using a versatile computer code that employs a matrix method to calculate the scattering at each interface and propagation through each layer. Mirrors and control samples are fabricated to design specifications using a multihead magnetron sputter system in which all process parameters are actively feedback-controlled. In this system, the mirror substrates undergo a

compound rotation during sputter deposition to ensure layer uniformity over the substrate area. After fabrication, the mirrors are screened for correct d and γ values using small-angle diffractometer measurements at the copper K_α line (~8 keV). Next, the mirrors are tested for x-ray reflectivity (and transmission, in the case of beamsplitters) at the wavelengths and incidence angles of interest at the Berlin electron storage ring synchrotron (called BESSY).

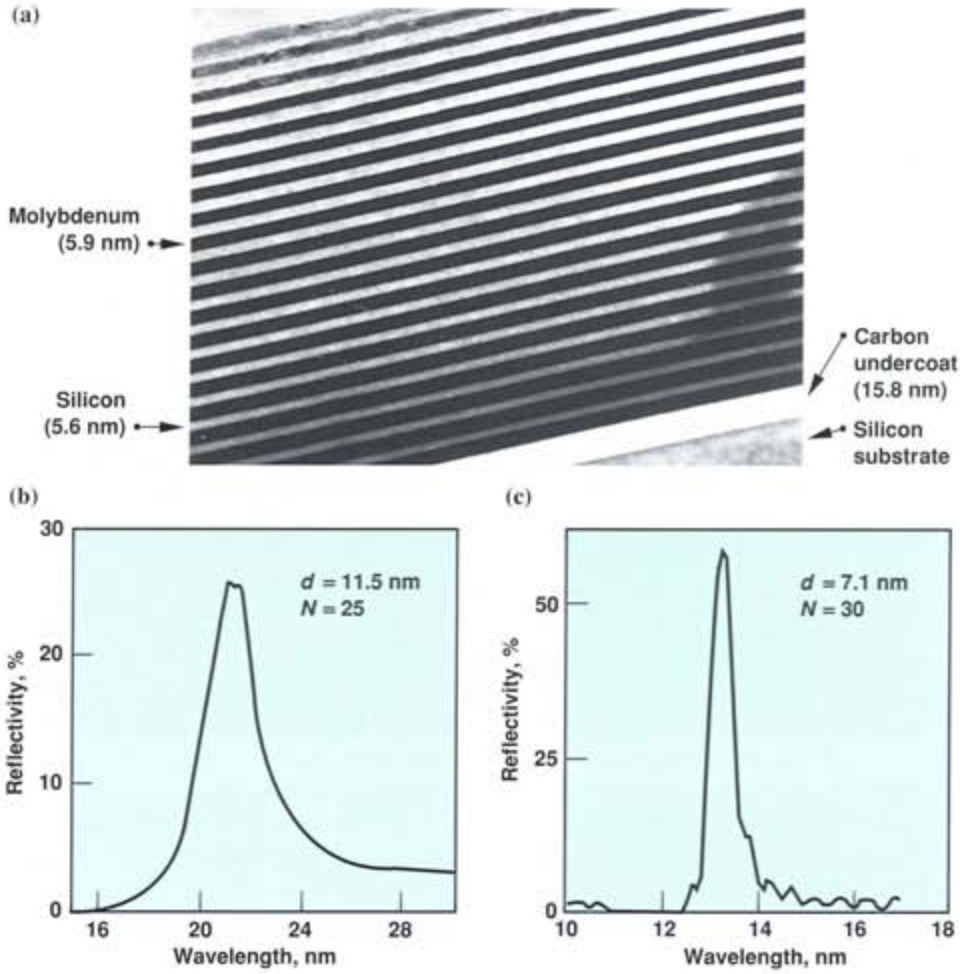

Figure 7. The current state of the art for x-ray mirrors in the spectral region from ~12.5 to ~22.0 nm. (a) A transmission electron micrograph of a molybdenum/silicon mirror with $d = 11.5$ nm, $\gamma = 0.51$, $N = 25$ designed for use at normal incidence in a cavity experiment on the neon-like selenium laser with ASE at 20.63 and 20.96 nm. (b) Measured reflectivity at virtual normal incidence (~0.5° off normal) for the mirror shown in (a). (c) Measured reflectivity (at ~0.5° off normal) for a mirror designed for use at normal incidence in a cavity experiment on the neon-like molybdenum x-ray laser with ASE at 13.1 and 13.27 nm. This mirror has $d = 7.1$ nm, $\gamma = 0.4$, and $N = 30$.

Control samples are sectioned and thinned for STEM analysis in order to inspect interface sharpness, layer-to-layer uniformity, and layer smoothness.

This detailed fabrication and characterization procedure has proved successful in producing molybdenum/silicon multilayer mirrors for x-ray laser research. Molybdenum and silicon are presently the materials of choice for mirrors in the spectral band from ~12.5 to 22.0 nm, where many of the laboratory x-ray lasers currently operate (Table 1). The molybdenum/silicon system exhibits good long-term stability and has layer interfaces that are reasonably sharp and well defined. In addition, silicon has L absorption edges at ~12.3 nm, so that its absorption is low for wavelengths greater than 12.5 nm, providing the possibility of fairly efficient mirrors at these wavelengths.

Figure 7 illustrates the current state of the art for x-ray mirrors in the spectral region from ~12.5 to 22.0 nm. Figure 7a shows a transmission-electron-microscope (TEM) image of a molybdenum/silicon mirror ($d = 11.5$ nm, $\gamma = 0.51$, $N = 25$) designed for use at normal incidence in a cavity experiment on the neon-like selenium x-ray laser with ASE at 20.63 and 20.96 nm. Figure 7b shows the measured reflectivity of that same mirror at virtual normal incidence (~0.5° off normal). The peak reflectivity of 28% occurs at 21.0 nm, and the mirror bandpass (FWHM) is 2.5 nm. Figure 7c shows the measured reflectivity (at ~0.5° off normal) for a different molybdenum/silicon multilayer mirror ($d \sim 7.1$ nm, $\gamma \sim 0.4$, $N = 30$) designed for use at normal incidence in a cavity experiment on the neon-like

molybdenum x-ray laser with ASE at 13.1 and 13.27 nm. The peak reflectivity of 59% occurs at 13.1 nm, and the mirror bandpass (FWHM) is ~1.0 nm.

From Figure 7 we see that over the spectral range from ~12.5 to 22.0 nm it is indeed possible to design, fabricate, and characterize efficient, high-quality multilayer mirrors. Multilayer-mirror capabilities at shorter wavelengths are not yet so well developed. However, the emergence of high-brightness x-ray sources and new applications are motivating an active effort in this area.

Beamsplitters

Another multilayer optical component of great interest is the soft-x-ray beamsplitter. At visible wavelengths, beamsplitters play a vital role in holographic, interferometric, and schlieren systems. They are important as output couplers for laser cavities, they are useful for beam-monitoring functions, and in general they provide versatility in sophisticated optical designs.

At LLNL, we have pioneered the development of multilayer beamsplitters for use at soft-x-ray wavelengths. Using silicon nitride membrane technology, originally developed by the integrated circuit industry for x-ray lithography, we have designed, fabricated, and tested molybdenum/silicon multilayers supported by thin (~30 nm), x-ray-transparent, silicon nitride membranes. In brief, a polished silicon wafer is coated (by chemical vapor deposition) with a thin silicon nitride film; a molybdenum/silicon multilayer is then deposited by magnetron sputtering onto the silicon nitride film. Using conventional patterning and anisotropic etching techniques, the underlying silicon wafer is removed from an area typically 10–20 mm^2, leaving a window of molybdenum/silicon multilayer supported by silicon nitride. The window is partially reflecting and transmitting, as illustrated in Figure 8.

Currently, the major obstacle to producing high-optical-quality beamsplitters for soft x rays is the roughness of the interface between

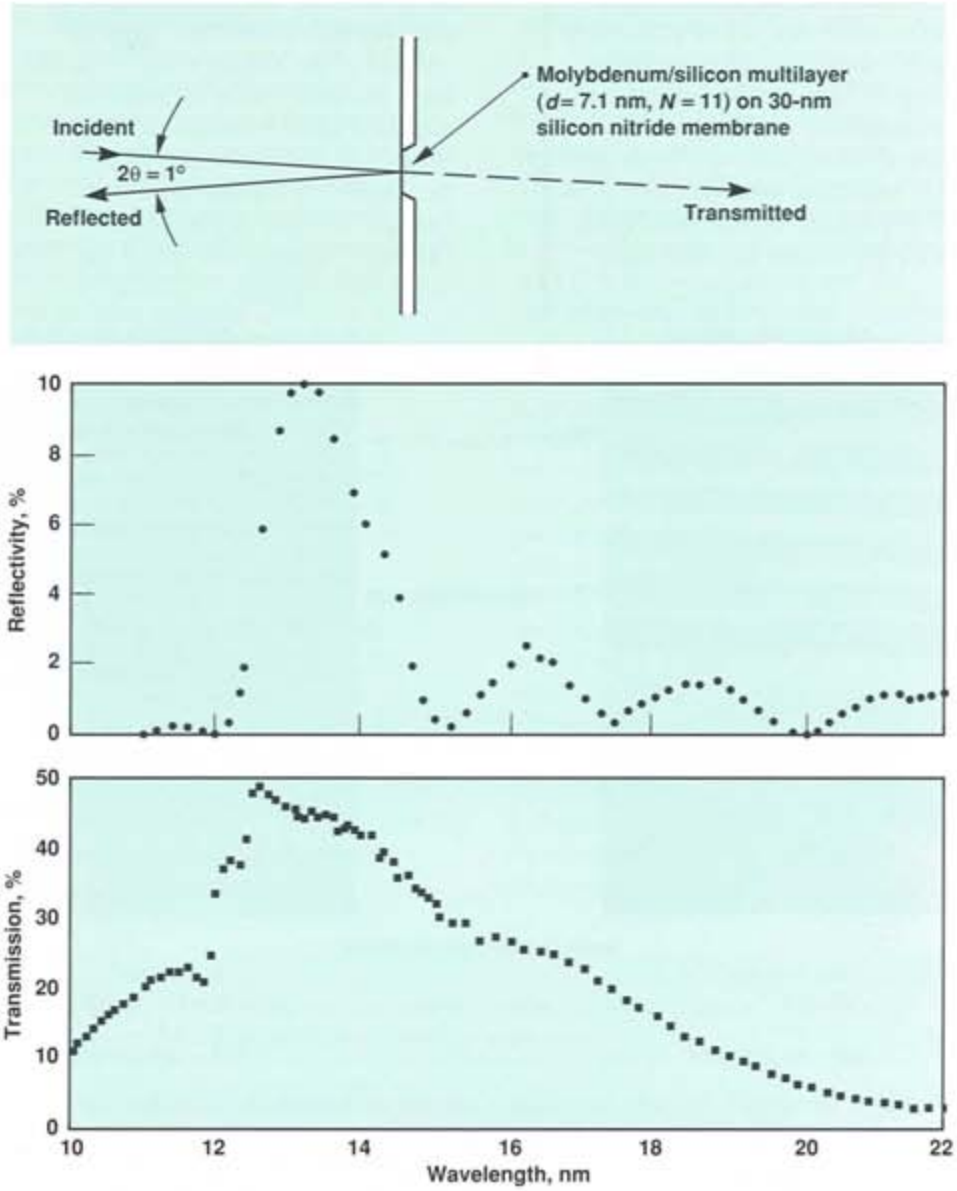

Figure 8. Soft-x-ray beamsplitters—the analog of "two way" optical mirrors—have been developed using multilayer technology. A schematic illustration of the performance of such a multilayer beamsplitter is shown, along with plots of measured (at ~0.5° off normal) reflectivity and transmission for a beamsplitter designed for use at 13.1 nm.

the silicon nitride (or other transparent support membrane) and the multilayer structure. It is not uncommon for the silicon nitride film to have a surface roughness of 1.0–1.5 nm. The roughness is replicated in the multilayer structure, reducing reflectivity and possibly distorting the wavefront of the reflected beam. While efforts are under way to produce smoother support films, improvements in beamsplitter performance have already been achieved by depositing the multilayer onto the back side of the silicon nitride membrane, after the silicon has first been anisotropically etched. In this procedure, the silicon nitride film is deposited onto the highly polished silicon wafer. The interface between the silicon nitride and the silicon appears to be almost as smooth as the polished wafer. After the silicon has been etched away, the molybdenum/ silicon multilayer is then deposited onto the "smooth" surface of the silicon nitride that had been in contact with the polished silicon. Figure 9 compares TEM images of molybdenum/silicon beamsplitters deposited on the "rough" top side (a) and on the "smooth" bottom side (b) of the silicon nitride. The reduced roughness in the bottom-deposited multilayers is clearly visible.

Figure 10 compares the performance of top- and bottom-deposited multilayers to that of a multilayer deposited onto a bare, highly polished silicon wafer. All samples were prepared in the same run of the magnetron sputter system. Nominally they are all molybdenum/ silicon multilayers with $d = 6.5$ nm, $\gamma \sim 0.3$, and $N = 13$. As shown, peak reflectivities are 17%, 13.4%, and 9.7% for the multilayers deposited

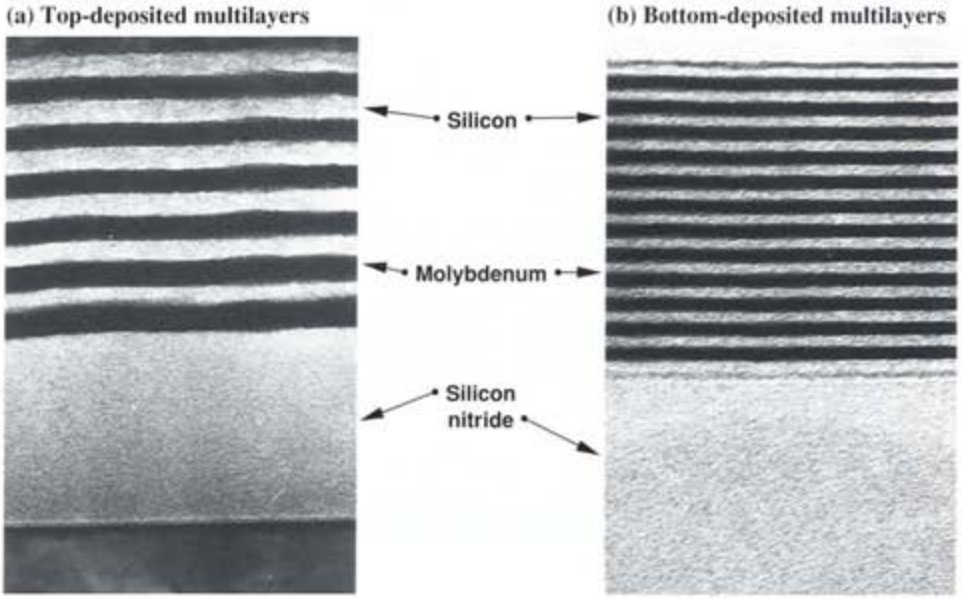

Beamsplitter specifications

$d = 11.5$ nm	$d = 6.5$ nm
$N = 7$	$N = 13$
$\gamma \sim 0.51$	$\gamma \sim 0.4$
SiN ~ 44 nm thick	SiN ~ 300 nm thick

Figure 9. Techniques are being developed to improve the flatness and smoothness of beamsplitter multilayer structures, and thereby improve beamsplitter performance. Comparative TEM images of molybdenum/silicon beamsplitter structures deposited on (a) the "rough" top side and (b) the "smooth" bottom side of silicon nitride membranes are shown. The improvements in multilayer smoothness and beamsplitter performance are evident in (b) and in Figure 10, respectively.

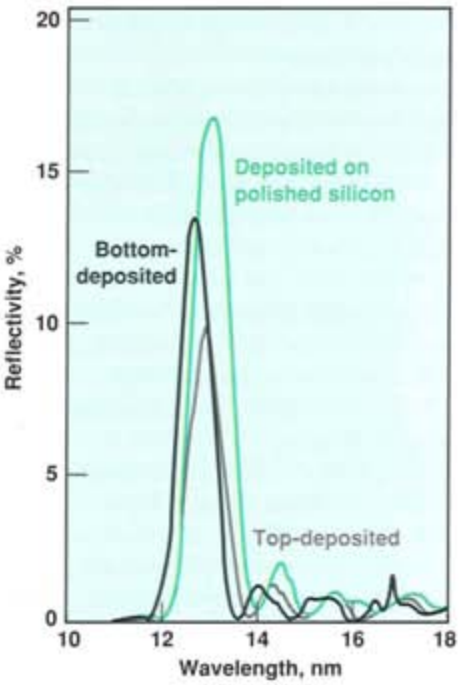

Figure 10. A comparison of x-ray performance for nominally identical multilayer structures deposited onto a polished silicon wafer, the bottom side of a silicon nitride membrane, and the top side of a silicon nitride membrane. As indicated in Figure 9, bottom deposition improves beamsplitter reflectivity, but the performance is not yet as good as that achieved with multilayers deposited onto highly polished substrates.

onto the polished wafer, bottom, and top sides of the silicon nitride, respectively. These results indicate that the the bottom-deposited beamsplitters, while better than top-deposited optics, are not yet as good as that of multilayers deposited onto highly polished substrates. (The slight shift in the d spacing for the bottom-deposited multilayer is apparently due to shadowing of the substrate surface by the sidewalls of the etched silicon.)

The soft-x-ray beamsplitters are new optical components, still in the early stages of development. First-generation devices were developed for x-ray laser applications at ~20 and ~13 nm, and their performance has been limited by the poor optical quality of the silicon nitride support membranes. Current research is focused on extending beamsplitter operation to shorter wavelengths and on finding new x-ray-transparent support membranes that are both strong and optically smooth. In both these efforts, new technologies from the microfabrication industry are playing an important role.

Holographic Optical Components

Synthetically generated holographic optical components represent the ultimate in the application of modern computer and microfabrication technologies to the control and manipulation of electromagnetic radiation. At infrared and visible wavelengths, the value of synthetically generated holographic optical components is well established. At LLNL we have pioneered the development of these components for use at soft-x-ray wavelengths. We have combined nanometer-scale lithography techniques (ultraviolet-holographic, electron-beam, and x-ray lithography) with multilayer thin-film deposition capabilities to produce three-dimensional diffractive structures—structures that are best described as synthetically generated x-ray reflection holograms.

Specifically, we have patterned 100-nm linewidth linear gratings into and onto multilayers to produce high-efficiency, normal-incidence reflection gratings. We have also patterned micro-Fresnel zone plates onto multilayers to produce planar focusing mirrors. In principle, using electron-beam lithography, we can pattern multilayers in any generalized fashion allowing complete amplitude and phase control (if coherently illuminated), and thereby focus control, over the reflected x rays.

Fabrication of a holographic component starts with the deposition of a multilayer mirror onto an optically flat substrate (using magnetron sputtering). Typically, a 500-nm thick layer of resist (a material that protects the surface from etching agents) is then deposited atop the multilayer mirror, and a submicrometer linewidth pattern (generated by ultraviolet-holographic or electron-beam lithography) is replicated into the resist. The top of the resist pattern is subsequently coated (by oblique-angle evaporation) with aluminum or chromium and is then used as a pattern mask for subsequent reactive-ion etching into the multilayer. The molybdenum/silicon multilayer is etched using a gas mixture of $CClF_3$ and oxygen.

Figure 11 is a TEM image of a sectioned and thinned piece of a grating-in-multilayer pattern. The grating period is 300 nm; the multilayer is molybdenum/silicon with $d = 11.3$ nm, $\gamma \sim 0.4$, and $N = 30$. Note the remarkable control over structural detail, as evidenced by the layer-to-layer uniformity, the sharp interfaces between the molybdenum and silicon layers, the edge definition of the grating pattern provided by precise etch control, the very few damaged layers, and the lack of residue in the etched regions.

We have characterized the x-ray performance of such grating-in-multilayer holographic optical components at the BESSY synchrotron in Berlin. The results from such a measurement are presented in Table 3. Shown are the measured diffraction efficiencies into the zero-through-fourth orders for a molybdenum/silicon multilayer with $d = 6.5$ nm, $\gamma \sim 0.3$, $N = 30$, into which is etched a linear grating pattern with a period p of 1 μm, a reflecting line/space of ~1.1, and illuminated at virtual normal incidence (~0.8° off normal) at 13 nm. A control mirror, fabricated on the same run, was measured to

Table 3. **Comparison of measured and calculated performance at 13 nm of a grating-in-multilayer holographic optical component.**

Diffracted order	Diffraction efficiency, %	
	Measured	Calculated
0	11.3	12.0
1	4.5	4.4
2	0.04	0.03
3	0.24	0.46
4	0.05	0.03

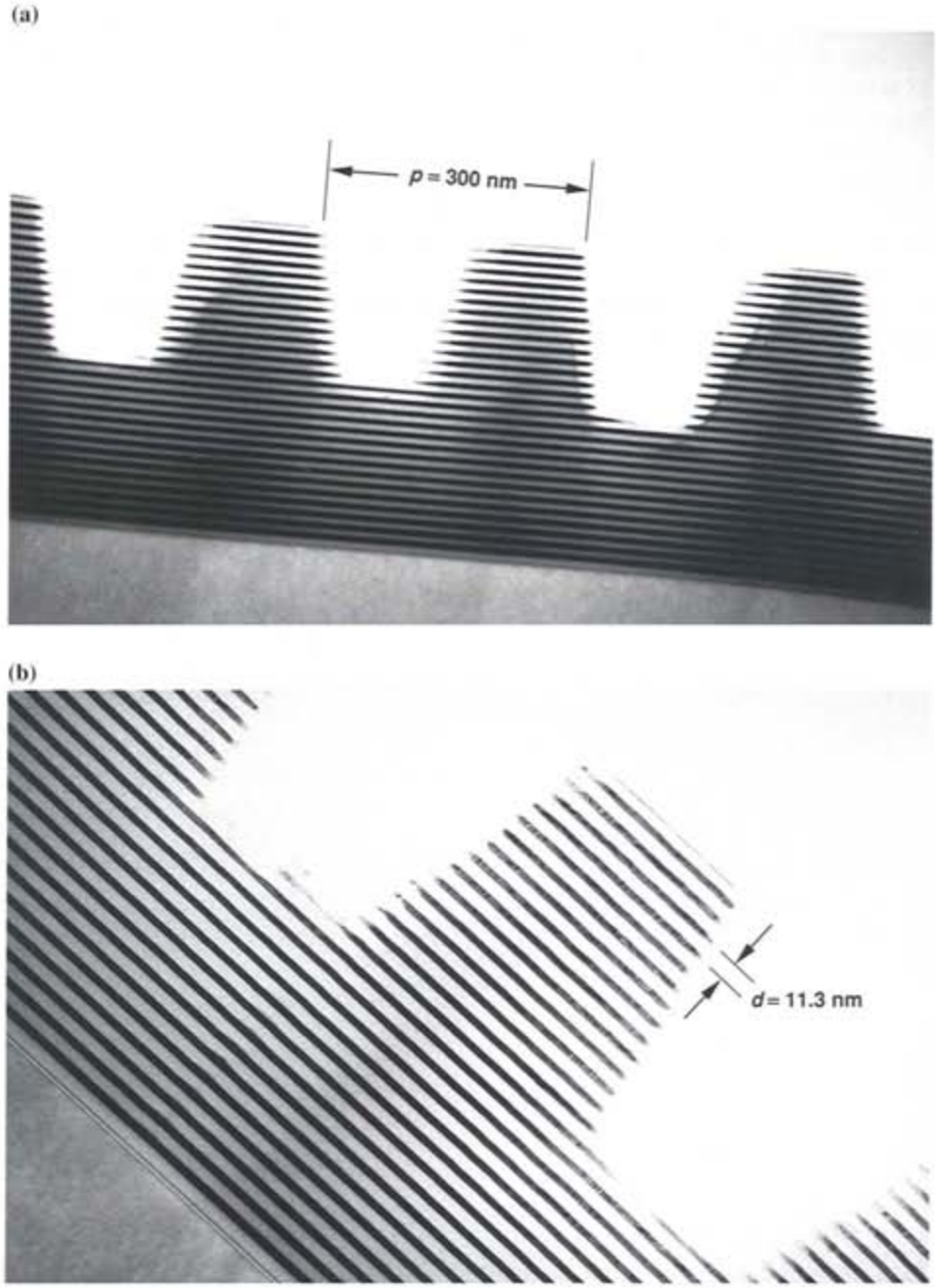

Figure 11. The marriage of nanolithography and multilayer technologies is allowing us to fabricate three-dimensional diffractive structures, such as the molybdenum/silicon structure shown here. These TEM micrographs, shown at two different magnifications in (a) and (b), are of a 300-nm-period linear grating etched into a multilayer with $d = 11.3$ nm, $\gamma = 0.4$, and $N = 30$.

have a normal-incidence reflectivity of 43.5% at 13 nm. From this value, we can calculate the expected diffraction efficiency values from an ideal linear reflection grating with the above characteristics. These calculated (theoretical) values are also listed in Table 3.

The good agreement between the measured and calculated diffraction efficiency values at low orders is strong testimony to our ability to fabricate high-quality holographic optical elements for soft-x-ray wavelengths. The disagreement at higher orders is probably due to sidewall taper in the real structures that is not accounted for in the calculations.

Detectors

Significant progress has been made in the development of time-, space-, and energy-discriminating x-ray detectors. Here we highlight two advanced x-ray detection systems—an x-ray CCD (charged-coupled device) camera and an ultrafast framing camera—that have particularly benefited from recent advances in semiconductor and ultrafast electronics.

X-Ray CCD Camera

X-ray CCDs are the x-ray analog of optical video imagers. They provide direct electronic x-ray detection over a two-dimensional field with low noise, high sensitivity, good dynamic range, high spatial resolution, extreme positional stability, real-time readout, and a capability for nondispersive energy discrimination.

The x-ray CCD is a silicon-based, two-dimensional detector array with its own information storage and transfer capability. Physically, it is a thin silicon wafer with appropriately

patterned layers of dopant, insulator, and conducting gate structures on its surface, making for a two-dimensional array of MOS (metal-oxide semiconductor) capacitor wells (i.e., detector pixels).

An x ray incident on this device will be absorbed (i.e., detected) in the silicon, producing a number of secondary electrons proportional to the x-ray energy. This discrete charge packet will be localized in the pixel (i.e., MOS capacitor) where the x ray was absorbed. By virtue of the CCD architecture, the spatial distribution of discrete charge packets (i.e., the image) can be electronically transferred (by clocking voltages applied to the gate electrodes) in an orderly fashion through the array and directly into digital computer memory.

At the current state of the art, CCDs are attractive as high-density ($\sim 2 \times 10^5/cm^2$) arrays of low-noise, individual silicon detectors with fairly rapid readout time (on the order of seconds). As detectors of the future, they have the added advantage of being closely coupled to advances in the microelectronics industry, which virtually assures rapid progress toward even higher quality, higher information density, lower noise, and more rapid readout devices.

An embodiment of the modern x-ray CCD camera is a system developed by Ricker, Doty, Luppino, and coworkers at the Massachusetts Institute of Technology as a focal-plane imager for an x-ray telescope to be flown by NASA in the 1990s. It is currently being used in modified form at LLNL as a laboratory detection system for characterizing high-resolution, grazing-incidence reflection optics for laser fusion research.

The specific imager chip used in this camera is the TI4849 virtual-phase CCD manufactured by Texas Instruments Corporation; its main structural features are illustrated in Figure 12. It has a full well capacity of $\sim 3 \times 10^5$ electrons (i.e., $\sim 10^3$ 1-keV x rays will saturate a pixel),

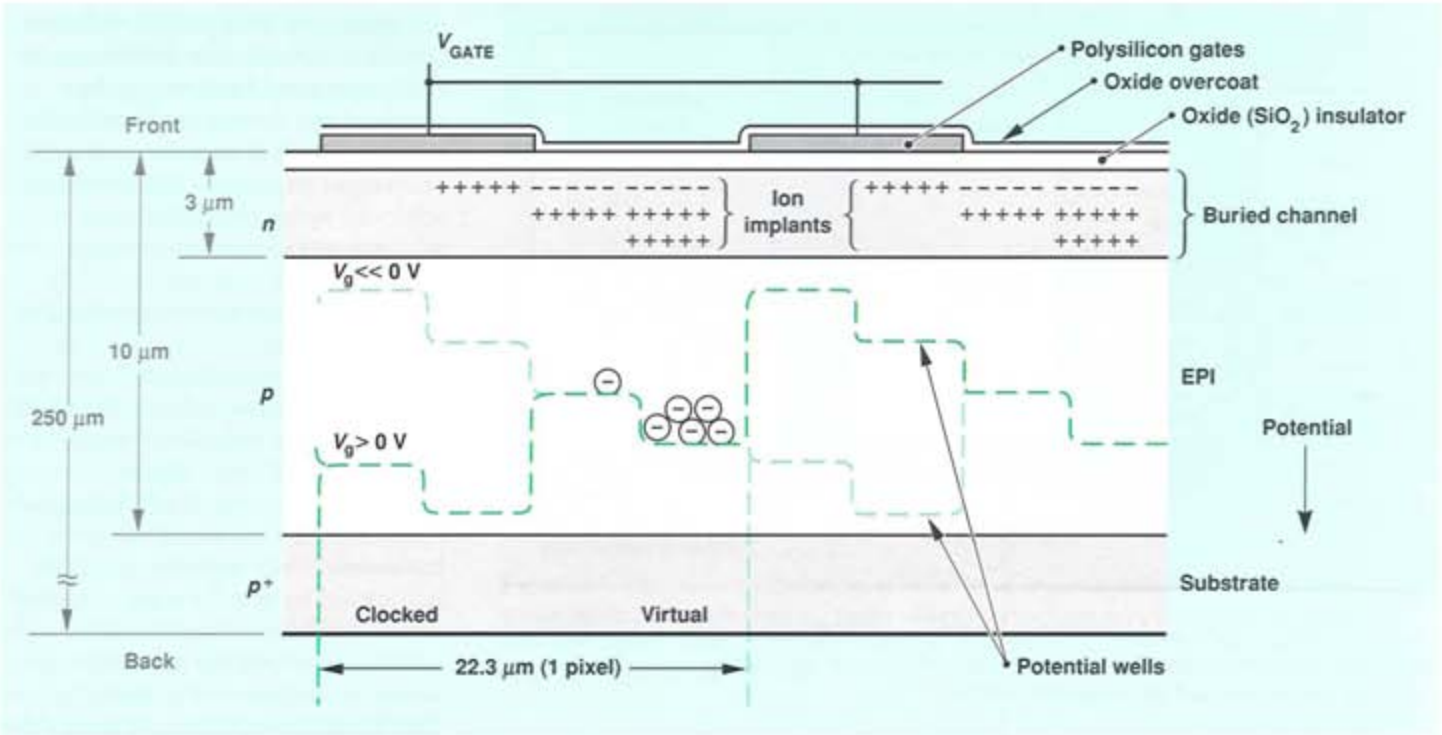

Figure 12. X-ray-sensitive CCD imagers are fast becoming the detectors of choice in a wide variety of x-ray imaging applications. The main structural features of the TI4849 virtual-phase CCD manufactured by Texas Instruments Corporation are shown here. The virtual-phase pixel is divided into two distinct regions: clocked and virtual. A fixed-potential well is formed in the silicon under the virtual region of the pixel due to the presence of the *n*-type ion implants ("+" signs). The clocked region is covered by a polysilicon gate; the voltage on this gate is controlled by a single external clock. The stepped potential under this gate moves up and down with respect to the pinned potential in the virtual region, thereby implementing charge transfer. Note that the virtual region is essentially bare except for a thin oxide overcoat and oxide insulator. This structure allows detection of x rays with energies as low as carbon K_α (277 eV).

a dark current of $<10^{-11}$ A/cm^2 at room temperature, an oxide layer of <80 nm (important for soft-x-ray sensitivity), and excellent pixel-to-pixel uniformity.

The CCD is an "unthinned," front-side-illuminated device with 22 × 22-μm pixels arranged in a 584 (vertical) × 390 (horizontal) array. Charge packets are clocked down vertical columns into a serial register, where they are clocked horizontally, pixel by pixel, to the on-chip MOSFET (metal-oxide semiconductor field-effect transistor) preamplifier. Sophisticated clocking and control electronics have reduced device readout noise to <8 electrons (rms) and have provided charge transfer efficiencies of >0.99999 (parallel) and >0.99998 (serial).

The overall architecture of this camera system and main subsystems is shown in Figure 13. The camera head contains the CCD chip, preamplifier electronics, vacuum system, and cooling system (either liquid-nitrogen cryostat or thermoelectric coolers). The TI4849 can provide optimal operation over a broad temperature range extending from –30 to –90°C. The front-end electronics perform all the control operations for the CCD; it generates the clock voltages that shift the charge out of the CCD, performs the low-noise amplification, signal processing, and A/D conversion of the CCD output signal, and transmits the digitized data to the computer system for display, analysis, and storage. The computer system (a DEC VAXstation II) provides keyboard control over the imaging functions of the camera, enabling the user to obtain images or spectra. An extensive interactive software package allows quasi-real-time data processing and manipulation of images and spectra.

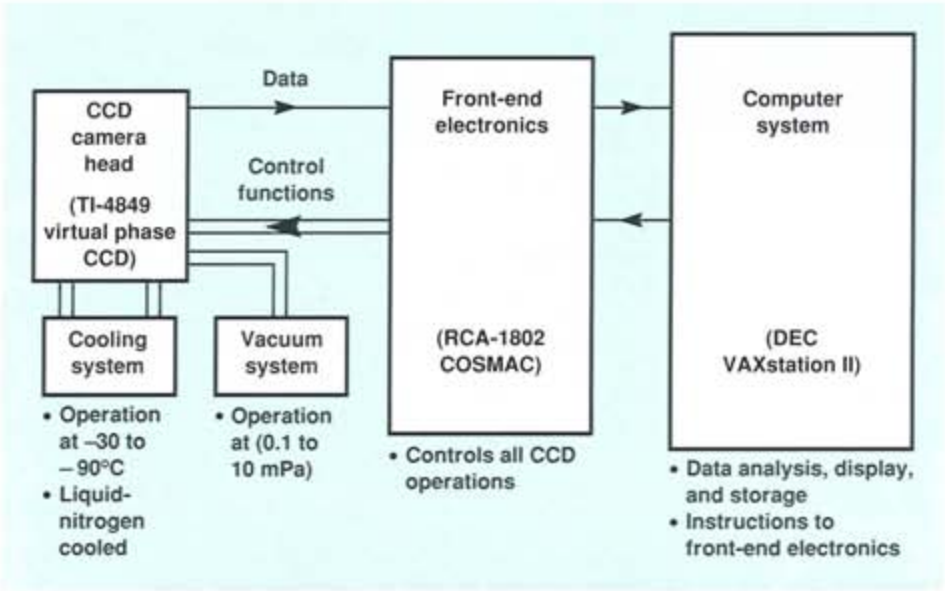

Figure 13. The overall architecture of the LLNL x-ray CCD camera system, showing the three main subsystems: the CCD camera head with vacuum and cooling apparatus, the front-end electronics, and the computer system.

The CCD camera's combined features of high-sensitivity (single photon detection for x-ray energies >270 eV), low noise, proportionality between x-ray energy and signal (number of secondary electrons), and real-time computer control of exposure function and data analysis, allow it to be used as a versatile, nondispersive imaging spectrometer. Detailed spectral information can be easily extracted from image data acquired in a "low-signal" mode, in which no pixel detects more than one photon per exposure. This can be achieved by programming data acquisition via many successive, short exposures and appropriately storing the data for subsequent pulse-height analysis.

Data illustrating the spectroscopic and imaging capabilities of the CCD camera are presented in Figures 14 and 15, respectively. Figure 14 shows characteristic K_α fluorescence spectra from a variety of targets bombarded with high-energy alpha particles. The spectra were recorded using the TI4849 chip cooled to –40°C, for which the system noise was ~10 electrons (rms) per pixel. The top curve in Figure 14 shows the detector's sensitivity to carbon K_α x rays at ~277 eV. (The soft-x-ray

sensitivity of the CCD is limited by its oxide layer.)

CCD imaging data are presented in Figure 15. Shown are segments of a Fresnel zone plate backlighted by 2.3-keV x rays and imaged onto the CCD by a Wölter Type I x-ray microscope with 22× magnification (1 pixel at the CCD image is equivalent to 1 μm at the source). Below the images are plots of CCD signal vs linear distance at the source. These illustrate the dimensional fidelity, edge definition, and contrast of the images. The smallest zone width imaged was ~10 μm.

The modern x-ray CCD camera has quickly become the detector of choice for sophisticated applications in x-ray astronomy. With its versatility, high-quality imaging characteristics, and capabilities for spectroscopy and real-time data acquisition and analysis, the x-ray CCD camera is also well suited for high-resolution (10-nm to 1-μm) x-ray microscopy and other advanced imaging applications.

X-Ray Framing Camera

The LLNL x-ray framing camera provides a two-dimensional x-ray imaging capability with a ~50-ps frame time for high spatial and temporal resolution of fast dynamical processes that emit or are probed by x rays.

X-ray investigation of ultrafast dynamical processes (e.g., laser-matter interactions, inertially confined fusion implosions, high-energy shock phenomena) requires such a highly specialized detection

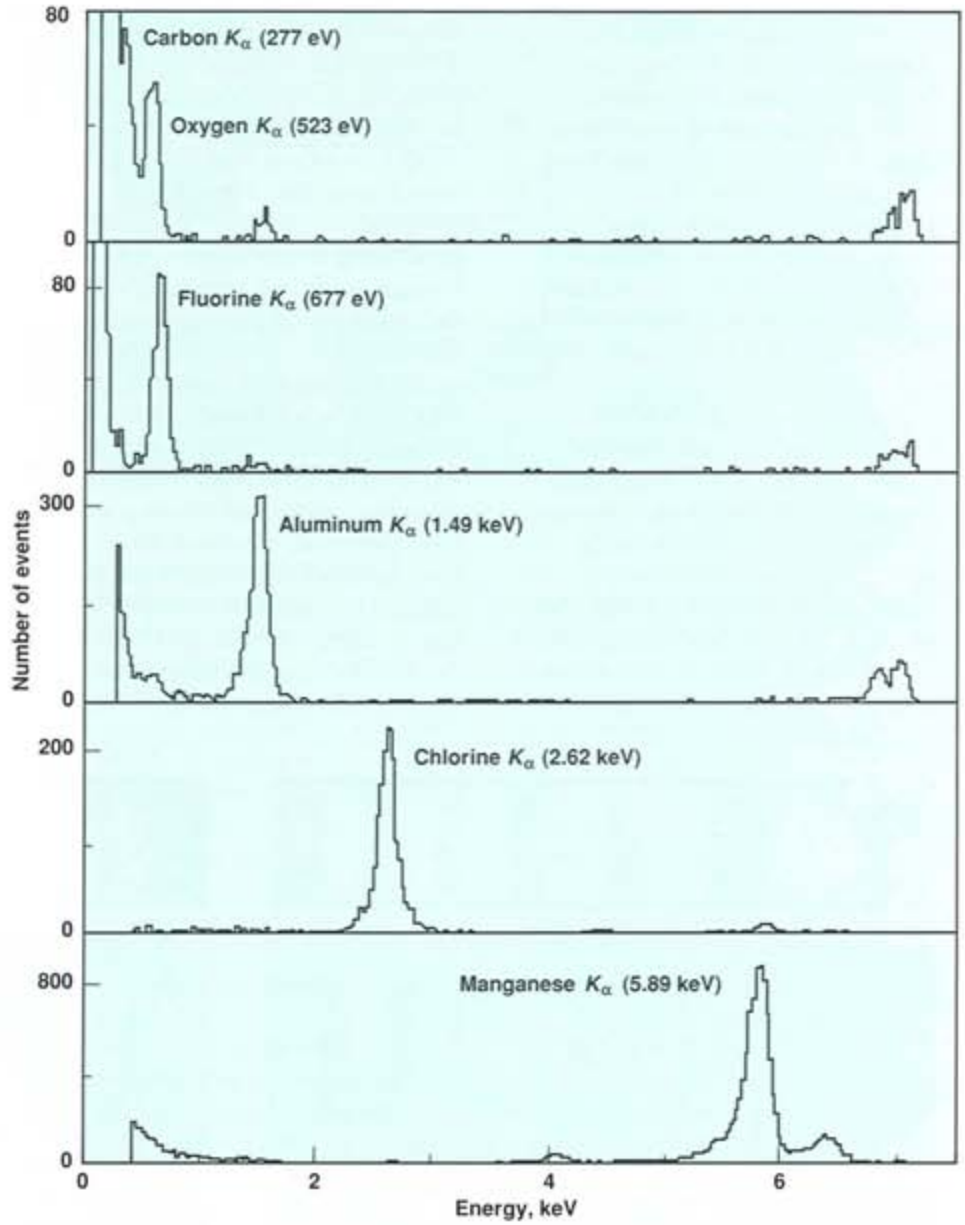

Figure 14. The x-ray CCD camera can also be used as a nondispersive x-ray spectrometer. Characteristic K_α fluorescence spectra from a variety of targets bombarded with high-energy alpha particles are shown. The top curve shows the detector's sensitivity to carbon K_α x rays at ~277 eV.

system. The x-ray framing camera was recently developed by Stearns and colleagues at LLNL for the investigation of laser-driven fusion implosions. Using a novel electro-optical gating system, the x-ray framing camera provides two-dimensional frames or "snapshots" of fast processes with a frame time of ~50 ps and a spatial resolution of ~22 μm over a 8.6 × 12.8-mm image field.

Figure 16 is a diagram of the x-ray framing camera design and operation. X rays are incident on a transmission photocathode composed of a 100-nm-thick cesium iodide layer deposited on the interior surface of a thin beryllium foil. The photocathode is incorporated into a suspended-strip vacuum transmission line (a 25-mm-wide gold strip suspended 1 mm above a copper ground plane with an impedance of 18 Ω). Prior to triggering, the transmission line is reverse-biased at ~700 V to ensure that photoelectrons do not leave the photocathode.

A framed image is obtained by generating an ultrashort, high-voltage pulse that propagates down the transmission line and accelerates electrons from the photocathode across the gap to the ground plane. The pulse is produced on the transmission line using a simple pulse-shaping network, consisting of a short section of the suspended strip electrically isolated by a photoconductive (single-crystal gallium arsenide) switch. The charge line is energized with a −11-kV, 50-ns pulse, and the camera is triggered by illuminating the

Table 4. Performance of a single-frame prototype framing camera.

Characteristic	Performance
Frame duration	50 ps
Spatial resolution	22 μm (CCD limited)
Image area	390 × 584 pixels (CCD limited) 8.6 × 12.8 mm
Shutter ratio	>1000
Quantum efficiency	0.01–0.1
Dynamic range	>3000

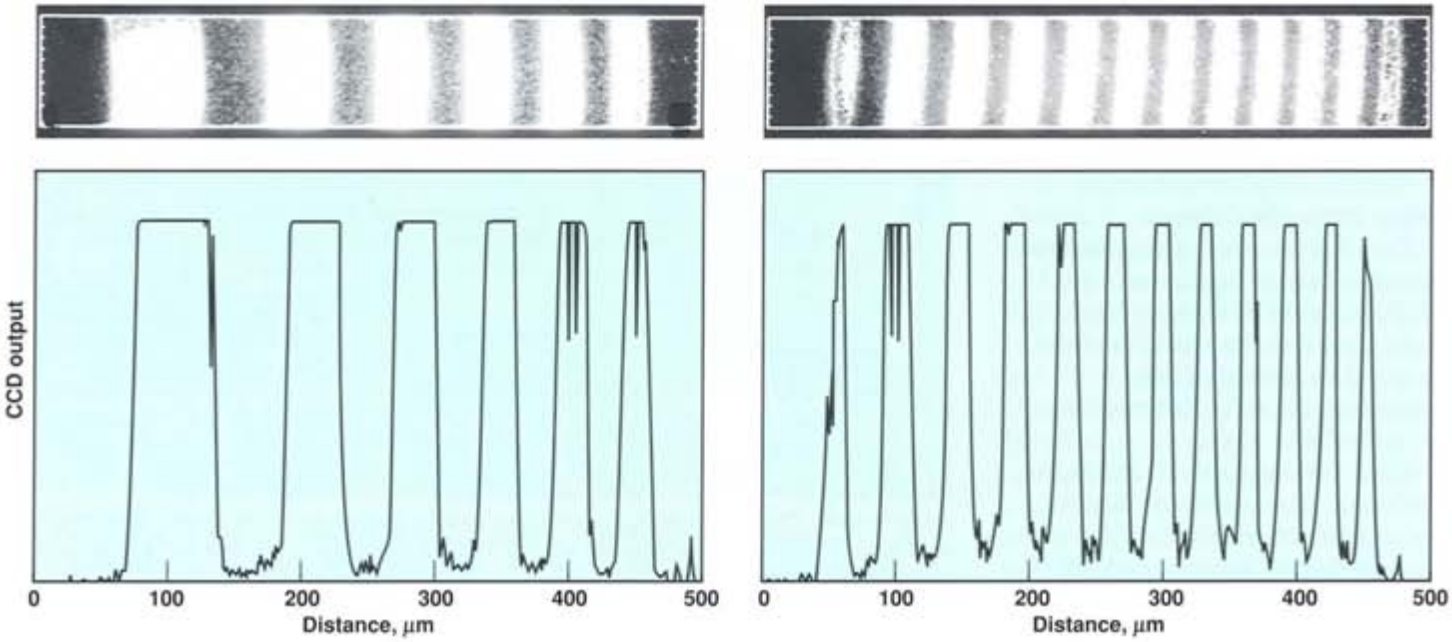

Figure 15. CCD image data. Shown are segments of a Fresnel zone plate backlighted by 2.3-keV x rays and imaged onto the CCD by a Wölter type-I x-ray microscope with 22× magnification (1 μm at the source = 1 pixel at the CCD image). Below the images are plots of CCD signal vs linear distance at the source, illustrating the dimensional fidelity, edge definition, and contrast of the images.

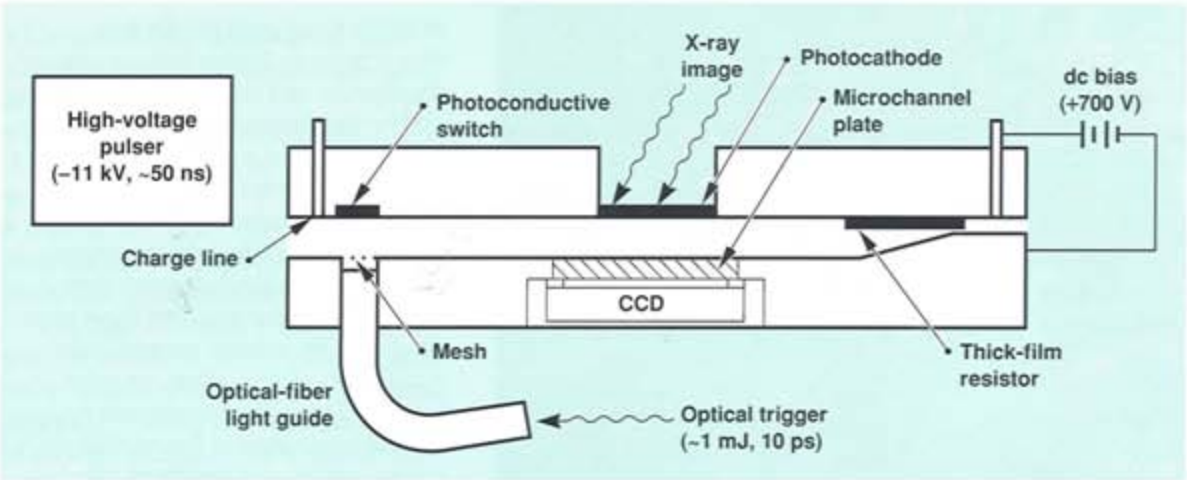

Figure 16. Schematic illustration of the design and operation of the x-ray framing camera recently developed at LLNL for the investigation of laser-driven fusion implosions.

photoconductive switch with a 10-ps, 250-μJ laser pulse through an optical-fiber light guide. Activating the photoconductive switch launches a voltage pulse down the transmission line, where it is ultimately absorbed in an impedance-matched, thin-film resistor at the end of the line. The launched pulse has half the 11-kV pulser voltage and is twice the temporal length of the charge line. As it traverses the photocathode, a photoelectron replica of the x-ray image (at the photocathode at that precise time) is accelerated across the transmission line gap toward the ground plane.

A microchannel plate, oriented to match the trajectory of the photoelectrons, is built into the ground plane and acts as a radiation filter, passing the photoelectron signal while blocking x rays that are transmitted through the photocathode. The photoelectron image passing through the microchannel plate is directly detected by a TI4849 CCD, which is coated with a thin layer of fluorescein dye to improve its quantum efficiency. The CCD is mounted within 1 mm of the microchannel plate for optimized spatial resolution. The framed image is readout electronically and stored on a microcomputer for subsequent analysis.

The measured performance characteristics of a single-frame prototype x-ray framing camera are presented in Table 4. The minimum frame duration is 50 ps. Spatial resolution at the image plane is 22 μm, limited by the CCD pixel size. The quantum efficiency of the camera (the number of detected photoelectrons per incident x-ray photon) is in the range 0.01–0.1 and is limited by the quantum efficiency of the photocathode. The camera dynamic range (i.e., ratio of saturation to SNR = 1, signal levels) is on the order of 3000, and the shutter ratio (i.e., triggered/untriggered signal levels) is approximately 1000.

The x-ray framing camera is an elegant application of a broad range of electro-optic technologies (photoconductive switches, CCDs, short pulse lasers, electro-optic sampling, etc.) to the solution of very challenging x-ray optical problems.